

# Free-Breathing Myocardial $T_1$ Mapping using Inversion-Recovery Radial FLASH and Motion-Resolved Model-Based Reconstruction

Xiaoqing Wang<sup>\*1,2,3</sup>, Sebastian Rosenzweig<sup>2,3</sup>, Volkert Roeloffs<sup>2</sup>,  
Moritz Blumenthal<sup>2</sup>, Zhengguo Tan<sup>2,3</sup>, Nick Scholand<sup>1</sup>, H.  
Christian M. Holme<sup>1</sup>, Christina Unterberg-Buchwald<sup>2,3</sup>, Rabea  
Hinkel<sup>3,5,6</sup>, and Martin Uecker<sup>1,2,3,4</sup>

<sup>1</sup>Institute of Biomedical Imaging, Graz University of Technology,  
Graz, Austria

<sup>2</sup>Institute for Diagnostic and Interventional Radiology of the  
University Medical Center Göttingen, Germany

<sup>3</sup>German Centre for Cardiovascular Research (DZHK), Partner  
Site Göttingen, Germany

<sup>4</sup>Cluster of Excellence “Multiscale Bioimaging: from Molecular  
Machines to Networks of Excitable Cells” (MBExC), University of  
Göttingen, Germany

<sup>5</sup>Laboratory Animal Science Unit, Leibniz Institute for Primate  
Research, Deutsches Primatenzentrum GmbH, Göttingen,  
Germany

<sup>6</sup>Institute for Animal Hygiene, Animal Welfare and Farm Animal  
Behavior, University of Veterinary Medicine, Hannover, Germany

July 18, 2022

## Abstract

**Purpose:** To develop a free-breathing myocardial  $T_1$  mapping technique using inversion-recovery (IR) radial fast low-angle shot (FLASH) and calibrationless motion-resolved model-based reconstruction.

**Methods:** Free-running (free-breathing, retrospective cardiac gating) IR radial FLASH is used for data acquisition at 3T. First, to reduce the waiting time between inversions, an analytical formula is derived that takes

---

\*Xiaoqing Wang, Institute of Biomedical Imaging, Graz University of Technology, Stremayrgasse 16/III, 8010 Graz, Austria. xiaoqingwang2010@gmail.com

the incomplete  $T_1$  recovery into account for an accurate  $T_1$  calculation. Second, the respiratory motion signal is estimated from the k-space center of the contrast varying acquisition using an adapted singular spectrum analysis (SSA-FARY) technique. Third, a motion-resolved model-based reconstruction is used to estimate both parameter and coil sensitivity maps directly from the sorted k-space data. Thus, spatio-temporal total variation, in addition to the spatial sparsity constraints, can be directly applied to the parameter maps. Validations are performed on an experimental phantom, eleven human subjects, and a young landrace pig with myocardial infarction.

**Results:** In comparison to an IR spin-echo reference, phantom results confirm good  $T_1$  accuracy, when reducing the waiting time from five seconds to one second using the new correction. The motion-resolved model-based reconstruction further improves  $T_1$  precision compared to the spatial regularization-only reconstruction. Aside from showing that a reliable respiratory motion signal can be estimated using modified SSA-FARY, in vivo studies demonstrate that dynamic myocardial  $T_1$  maps can be obtained within two minutes with good precision and repeatability.

**Conclusion:** Motion-resolved myocardial  $T_1$  mapping during free-breathing with good accuracy, precision and repeatability can be achieved by combining inversion-recovery radial FLASH, self-gating and a calibrationless motion-resolved model-based reconstruction.

**Keywords:** myocardial  $T_1$  mapping, model-based reconstruction, radial FLASH, spatio-temporal total variation

## 1 Introduction

Quantitative myocardial  $T_1$  mapping is becoming more and more important in clinical cardiovascular magnetic resonance (CMR) imaging [1, 2]. For example, both native and post-contrast  $T_1$  mapping can be used to assess diffuse myocardial fibrosis [3]. Commonly used  $T_1$  mapping techniques are modified Look-Locker inversion recovery (MOLLI) [4], saturation recovery single-shot acquisition (SASHA) [5], and saturation pulse prepared heart rate independent inversion recovery (SAPPHIRE) [6]. These techniques normally utilize a breathhold to mitigate respiratory motion and use an external electrocardiogram (ECG) device to synchronize data acquisition to a certain cardiac phase (e.g., end-diastolic), reducing the influence of cardiac motion. Although widely used, the need of a breathhold time of around 11 to 17 heartbeats may cause discomfort for patients (such as heart failure patients) and limits the achievable spatial resolution. Substantial efforts were made to shorten the breathhold period by optimized sampling [7], or by using non-Cartesian acquisition for single-shot myocardial  $T_1$  mapping [8, 9, 10] or by cardiac magnetic resonance fingerprinting (MRF) techniques for efficient multi-parameter mapping [11, 12, 13, 14]. More recently, free-breathing strategies [15, 16, 17, 18, 19] were investigated. These approaches acquire data continuously without the need for breath-holding and extract motion (respiration and/or cardiac) signals from the measured data itself using self-gating techniques. Following motion-resolved im-

age reconstruction and pixel-wise fitting/matching, cardiac  $T_1$  maps can then be obtained for certain motion states.

Model-based reconstruction [20, 21, 22] is an alternative approach to quantitative MRI. These methods directly reconstruct parameter maps from k-space, substantially reducing the number of unknowns to the number of actual physical parameters by not first reconstructing contrast-weighted images. They also offer a flexible choice of temporal footprint for parameter quantification as no intermediate image reconstruction is needed. Furthermore, sparsity constraints can be applied directly to the parameter maps to improve precision [23, 24, 25]. Model-based approaches have been used to accelerate myocardial  $T_1$  mapping at high spatial resolution [26, 27], but still require breath-holding.

Combining idea from all these strategies, we aim to develop a free-breathing myocardial  $T_1$  mapping technique by combining a free-running inversion-prepared radial FLASH sequence, an adapted self-gating technique and a calibrationless motion-resolved model-based reconstruction. In particular, the techniques integrate three novel developments: First, instead of setting the delay long enough to allow for a full  $T_1$  recovery ( $> 5$  s), we have derived an analytical formula for accurate  $T_1$  calculation even when the  $T_1$  recovery is incomplete, i.e.,  $\leq 3$  s. Second, to allow for robust respiratory motion estimation, we propose to use an extended technique based on SSA-FARY [28] to extract the respiratory motion signal from the k-space center by eliminating the trajectory-dependent oscillations and inversion contrast in a preprocessing step. Third, after sorting raw data into a number of respiration and cardiac bins based on the estimated respiration signal and the recorded ECG signal, we estimate both parameter maps and coil sensitivity maps of the desired motion bins directly from k-space using a calibrationless motion-resolved model-based reconstruction. The latter is an extension of a previously developed model-based reconstruction [24, 27] to the motion-resolved case which enables the application of sparsity constraints along all motion dimensions, in addition to the spatial regularization, to further improve  $T_1$  precision. Validation of the proposed method was performed on an experimental phantom, eleven healthy subjects and one landrace pig with infarcted myocardium.

## 2 Theory

The free-running  $T_1$  mapping sequence (free-breathing, retrospective cardiac gating) is shown in Figure 1 (A). It consists of three repeated blocks: (1) non-selective inversion (2) a continuous radial FLASH readout using a tiny golden-angle ( $\approx 23.63^\circ$ ) [29] with a 3-s duration (3) and a time delay ( $T_1$  recovery) before the inversion in the next repetition. In previous studies using multiple inversions [30, 31], the delay time was set long enough to ensure a full recovery of longitudinal magnetization so that  $T_1$  can still be calculated using the conventional Look-Locker formula [32, 33]. However, a full recovery may need as long as 5 seconds for cardiac  $T_1$  mapping, which prolongs the total acquisition time. In this work, we treat this delay as a period that encodes  $T_1$  information in the

data. We use an analytical formula based on  $T_1$ ,  $T_1^*$ , the steady-state signal  $M_{ss}$ , and the new start magnetization signal  $M'_0$  (i.e., in the case that the  $T_1$  recovery is not complete:  $M'_0 < M_0$ , with  $M_0$  the equilibrium magnetization):

$$M'_0 = \frac{R_1 M_{ss} R_1^* (1 - E_1) + E_1 M_{ss} (1 - E_1^*)}{1 + E_1 \cdot E_1^*} \quad (1)$$

where  $E_1 = e^{-R_1 \cdot t_1}$ ,  $E_1^* = e^{-R_1^* \cdot t_{1s}}$ ,  $R_1 = 1/T_1$ ,  $R_1^* = 1/T_1^*$  and  $t_1$ ,  $t_{1s}$  are the time periods for  $T_1$  and  $T_1^*$  relaxation, respectively. Thus,  $T_1$  can be estimated even from partial  $T_1$  recoveries after reconstruction of the parameter maps  $(M_{ss}, M'_0, R_1^*)^T$  according to Equation (1). Here, we adopt a bisection root-finding algorithm to solve Equation (1). A full derivation of the above equation can be found in the Supporting Information File.

## Respiratory Motion Estimation

The main steps of the respiratory motion estimation process is demonstrated in the flowchart in Figure 1 (B). In the following, we explain all these steps in detail. Similar to [34, 28], we construct an auto-calibration (AC) region for self-gating using the central k-space samples of a radial acquisition, resulting in a time-series  $X(t)$  of size  $[N_C \times N_t]$ , with  $N_C$  and  $N_t$  the total number of channels (phased array coils) and central k-space points, respectively.  $N_t = N_S \cdot N_I$ , with  $N_S$  the number of sampling points per IR and  $N_I$  the total number of inversions. The AC data is usually corrupted by a trajectory-dependent signal due to eddy currents. Therefore, we first remove such oscillations by extending the method of orthogonal projections (with higher-order harmonics) from the steady-state case [28] to the contrast-change case (inversion recovery). Details of this procedure can be found in the Appendix I.

Following removal of the oscillations, the new k-space center signal  $\tilde{X}(t)$  can be modeled as

$$\tilde{X}(t) = s(t) \cdot m_1(t) + m_2(t) \quad (2)$$

with  $s(t)$  the steady-state signal which contains motion information (ideally without contrast change), and  $m_1(t)$  and  $m_2(t)$  the multiplicative and additive signals which model the contrast change due to inversion [35]. Here we propose the following procedure to remove the main effects from the changing contrast and to extract the signal component that is most relevant for respiratory motion:

- Step 1. Estimating  $m_2(t)$ : Perform the singular spectrum analysis (SSA) on  $\tilde{X}(t)$ , remove the components that are mostly related to the inversion-recovery contrast in the spectrum domain and transfer the processed signal back to the time domain. In SSA [28], this step largely removes the additive contrast-changing component of Equation (2), resulting in a new signal  $\tilde{X}_1(t) = \tilde{X}(t) - \tilde{m}_2(t)$ , with  $\tilde{m}_2(t)$  the estimated additive contrast-changing signal.
- Step 2. Estimating  $m_1(t)$ : Since the multiplicative component is mainly left in Equation (2), the singular value decomposition (SVD) is then performed on  $\tilde{X}_1(t)$  and the corresponding rank-one approximation is taken,

generating an estimate of the multiplicative component  $\tilde{m}_1(t)$ . Next, the magnitude of  $\tilde{m}_1(t)$  was utilized for the calculation, leading to a new signal  $\tilde{s}(t) = \frac{\tilde{X}_1(t)}{|\tilde{m}_1(t)|}$ . Due to the  $180^\circ$  phase difference before and after zero-crossing caused by inversion, the phase of  $\tilde{s}(t)$  before zero-crossing needs to be inverted. This was done by first detecting the minimum points of the signal  $\tilde{X}(t)$  (zero-crossing) for each coil and inversion and then correcting using:

$$\tilde{s}_1(t) = \begin{cases} -\tilde{s}(t), & \text{if } t \leq \text{zero-crossing} \\ \tilde{s}(t), & \text{otherwise.} \end{cases} \quad (3)$$

- Step 3. Zero-padding: To account for the missing temporal information due to the delay time between inversions,  $\tilde{s}_1(t)$  was zero-padded, generating a new signal  $\tilde{s}_2(t) \in C^{[N_C \times (N_I \cdot (N_S + N_Z))]}$  with  $N_Z$  calculated by  $N_Z = \frac{\text{Delay Time}}{\text{Repetition Time (TR)}}$ .
- Step 4. SSA-FARY: Perform SSA-FARY on  $\tilde{s}_2(t)$  with the window size tuned to estimate the signal component that is most relevant for the respiratory motion.

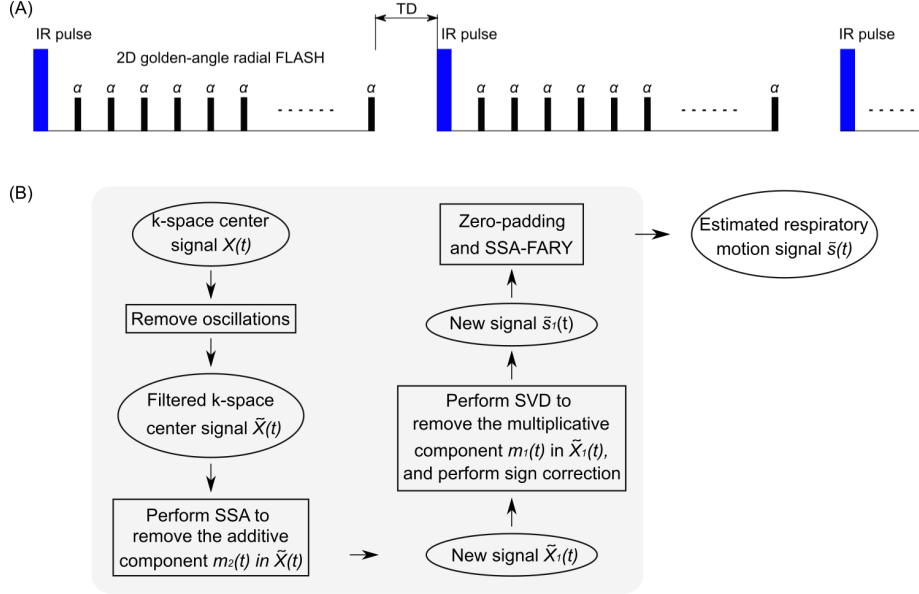


Figure 1: A. Schematic diagram of the free-running inversion-recovery radial FLASH sequence. Note TD is the delay time between inversions and this period encodes pure  $T_1$  information in the data. B. Flowchart of the main steps in the adapted SSA-FARY technique for the respiratory motion signal estimation from the k-space center.

## Motion-Resolved Model-Based Reconstruction

The acquired k-space data is then sorted into 6 respiration and 20 cardiac bins using amplitude binning [36] based on the estimated respiratory signal and the recorded ECG signal. The MR physical parameter maps in Equation (1) for the selected motion states are estimated directly from k-space using a calibrationless model-based reconstruction [24, 27]. Here, to further exploit sparsity along the motion dimensions, the previous model-based reconstruction is extended to the motion-resolved case by formulating the estimation of parameter maps and coil sensitivity maps from the selected motion states as a single regularized nonlinear inverse problem:

$$\hat{x} = \arg \min_{x \in S} \sum_{r=1}^{T_R} \sum_{c=1}^{T_C} \left\| F_{r,c}(x) - Y_{r,c} \right\|_2^2 + \alpha R(x_m) + \beta U(x_c) \quad (4)$$

where  $F$  is a nonlinear operator [27] mapping all unknowns  $x$  to the sorted k-space data  $Y$ .  $T_R, T_C$  are the numbers of respiration and cardiac bins, respectively.  $x = (x_m, x_c)^T$  where  $x_m$  contains MR physical parameter maps in Equation (1), i.e.,  $(M_{ss}, M_0, R_1^*)^T$  of all the selected motion states and  $x_c$  represents coil sensitivity maps  $(c_1, \dots, c_{N_C})^T$  for the corresponding motion states.  $S$  is a convex set ensuring non-negativity of the relaxation rate  $R_1^*$ . For the regularization  $R(\cdot)$ , we first adopt the joint  $\ell_1$ -Wavelet spatial constraints [24]. Second, we add the temporal total variation (TV) regularization to explore sparsity along the motion dimensions [37]. Furthermore, as a pure TV may favor straight lines if applied along the motion dimension only, we utilize a joint TV regularization along spatial and temporal dimensions to better preserve the spatio-temporal information. Thus,  $R(\cdot)$  reads:

$$R(x_m) = \lambda_1 \|Wx_m\|_1 + \sqrt{\lambda_2 \|D_x x_m\|^2 + \lambda_3 \|D_y x_m\|^2 + \lambda_4 \|D_c x_m\|^2 + \lambda_5 \|D_r x_m\|^2} \quad (5)$$

with  $\|Wx_m\|_1$  the joint  $\ell_1$ -Wavelet spatial regularization and  $D_x, D_y, D_a$  and  $D_r$  the gradient operators along the  $x, y$ , cardiac and respiratory dimensions, respectively.  $\lambda_1, \lambda_2, \lambda_3, \lambda_4$  and  $\lambda_5$  are the corresponding weighting parameters, balancing the effects of different regularization terms.  $\alpha$  is a global regularization parameter on  $R(\cdot)$ .  $U(\cdot)$  represents the Sobolev regularization term [38] on the coil sensitivity maps with  $\beta$  the regularization parameter. Similar to [24, 27], the above nonlinear inverse problem is solved by the iteratively regularized Gauss-Newton method (IRGNM) algorithm [39] where the nonlinear problem in Equation (4) is linearizedly solved in each Gauss-Newton step, i.e.,

$$\hat{x}_{n+1} = \arg \min_{x \in S} \sum_{r=1}^{T_R} \sum_{c=1}^{T_C} \left\| DF_{r,c}(x_n)(x - x_n) + F_{r,c}(x_n) - Y_{r,c} \right\|_2^2 + \alpha_n R(x_m) + \beta_n U(x_c) \quad (6)$$

with  $DF_{r,c}(x_n)$  the Fréchet derivative of  $F_{r,c}$  at the point  $x_n$  for the  $n$ th Gauss-Newton step. Here, the regularized least-squares subproblem (6) is solved by the ADMM algorithm [40] which enables the use of multiple regularizations. The

IRGNM-ADMM algorithm follows a similar structure as IRGNM-FISTA in [24]. For the sake of completeness, we include the pseudocode for the IRGNM-ADMM algorithm in Appendix II.

### 3 Methods

#### Data Acquisition

All MRI experiments were performed on a Magnetom Skyra 3T (Siemens Healthineers, Erlangen, Germany) with approval of the local ethics committee. Validations were first performed on a commercial reference phantom (Diagnostic Sonar LTD, Scotland, UK) consisting of 6 compartments with defined  $T_1$  values surrounded by water. Phantom scans employed a 20-channel head/neck coil, while in vivo measurements used a combined thorax and spine coils with 26 channels. In the phantom study, the delay time TD in the sequence was varied from 5 s to 1 s (with a step size of 1 s) to study  $T_1$  accuracy and precision when using the proposed  $T_1$  estimation procedure. An optimal value of TD was then chosen for subsequent in vivo studies. Informed written consent was obtained from all subjects prior to MRI. In vivo scans were performed during free-breathing using the free-running sequence. The ECG signals were recorded for later use but not for triggering. To assess repeatability of the proposed method, the sequence was repeated twice in the middle short-axis slice for each subject. Data from basal and apical slices were additionally acquired for a subset of subjects. After excluding measurements with non-reliable ECG signal, data sets from eleven subjects (seven female, four male, age  $25 \pm 4$ , range 21 - 37 years; heart rates  $63 \pm 9$  bpm, range 50 - 77 bpm) were used in this work (including six subjects with basal and apical slices). For FLASH readout, spoiling of the residual transverse magnetization was achieved using random radiofrequency (RF) phases [41]. The other acquisition parameters were: field of view (FOV) =  $256 \times 256$  mm<sup>2</sup>, slice thickness = 6 mm, matrix size =  $256 \times 256$ , TR/echo time (TE) = 3.27-3.30/1.98 ms, RF-pulse time-bandwidth product = 4.5, nominal flip angle = 6°, receiver bandwidth = 810 Hz/pixel and a total acquisition time of 21 inversions, i.e., around 2 min with 915 radial spokes per inversion. A window size of 21 frames was chosen for the adapted SSA-FARY technique [28]. Further, one data set from a young landrace pig with infarcted myocardium (regions in the septum and anterior wall due to intermittent left anterior descending artery occlusion) was acquired on the mid-ventricular short-axis slice using the same free-running acquisition parameters described above.

For reference, the gold standard  $T_1$  mapping was performed on the phantom using an IR spin-echo method [42] with 9 IR scans (TI = 30, 530, 1030, 1530, 2030, 2530, 3030, 3530, 4030 ms), TR/TE = 4050/12 ms, FOV =  $192 \times 192$  mm<sup>2</sup>, slice thickness = 5 mm, matrix size =  $192 \times 192$ , and a total acquisition time of 2.4 h. For in vivo studies, a 5(3)3 MOLLI reference sequence provided by the vendor was applied for end-diastolic  $T_1$  mapping using a FOV of  $360 \times 306.6$  mm<sup>2</sup>, in-plane resolution =  $1.41 \times 1.41 \times 8$  mm<sup>3</sup>, TR/TE = 2.7/1.12 ms, nominal

flip angle =  $35^\circ$ , receiver bandwidth = 1085 Hz/pixel and an acquisition period of 11 heart beats during a single breathhold.

## Iterative Reconstruction

The motion-resolved model-based reconstruction algorithm was implemented using the nonlinear operator and optimization framework in C/CUDA in the Berkeley Advanced Reconstruction Toolbox (BART) [43]. To reduce computational demand, we selected three respiratory motion bins (out of 6) close to the end-respiratory state and all cardiac bins for the motion-resolved quantitative reconstruction. Similar to [24], we initialized the parameter maps  $(M_{ss}, M'_0, R_1^*)^T$  with  $(1.0, 1.0, 1.5)^T$  and all coil sensitivities with zeros in the IRGNM-ADMM algorithm. Moreover, as a high accuracy is usually not necessary during the first Gauss-Newton steps, we set the number of ADMM iteration steps to be  $N_n = \min(100, 2N_{n-1})$  at the  $n$ -th Gauss-Newton step with  $N_0 = 10$ . This setting resulted in stable reconstructions for all cases tested.

Regularization parameters were tuned to balance the preservation of image details versus reduction of noise. The regularization parameters  $\alpha$  and  $\beta$  were initialized with 1.0 and subsequently reduced by a factor of three in each Gauss-Newton step. A minimum value of  $\alpha$  was used to control the noise of the estimated parameter maps even with a large number of Gauss-Newton steps, i.e.,  $\alpha_{n+1} = \max(\alpha_{\min}, (1/3)^n \cdot \alpha_0)$ . The optimal value  $\alpha_{\min}$  as well as the weighting parameters  $\lambda$ s were chosen manually to optimize the signal-to-noise ratio (SNR) without compromising the quantitative accuracy or delineation of structural details. Particularly,  $\alpha_{\min}$  was tuned from 0.004 to 0.007 with the optimal value chosen by visual inspection.  $\lambda_1$  was set to be 0.2 and parameters  $(\lambda_2, \lambda_3, \lambda_4, \lambda_5)^T$  in the weighted spatio-temporal TV regularization term in Equation (5) were set to be  $(0.4, 0.4, 1.0, 0.2)^T$ . For comparison, the other types of regularization, such as the spatial-only ( $\ell_1$ -Wavelet) regularization ( $R(x_m) = \lambda_1 \|W x_m\|_1$ ), temporal TV regularization ( $R(x_m) = \lambda_4 \|D_c x_m\|_1 + \lambda_5 \|D_r x_m\|_1$ ) and the combination of the above two ( $R(x_m) = \lambda_1 \|W x_m\|_1 + \lambda_4 \|D_c x_m\|_1 + \lambda_5 \|D_r x_m\|_1$ ) were also implemented and first evaluated on a simulated dynamic phantom using the parallel imaging and compressed sensing (PICS) tool in BART, followed by the evaluation on the data of one subject with the proposed motion-resolved model-based reconstruction. More details regarding the simulated dynamic phantom can be found in the Supporting Information File.

With the above parameter settings, all image reconstruction was done offline. After gradient-delay correction [44] and channel compression to six principal components, the multi-coil radial data were gridded onto a Cartesian grid, where all successive iterations were then performed using FFT-based convolutions with the point-spread function [45]. To reduce memory demand during iterations, 15 spokes were binned into one k-space frame prior to model-based reconstruction, resulting in a nominal temporal resolution of around 49 ms. To allow for efficient reconstructions, implementations were optimized in BART (see Appendix III) so that all computations could run on a GPU (A100, NVIDIA, Santa Clara, CA) with a memory of 80 GB. It then took around 20 - 30 minutes to reconstruct

one in vivo data set using the above reconstruction parameters.

## $T_1$ Analysis

All quantitative  $T_1$  results are reported as mean  $\pm$  standard deviation (SD). For the in vivo studies,  $T_1$  maps from the end-diastolic and end-respiratory phase were selected for quantitative assessment of the proposed method. Regions-of-interest (ROIs) were carefully drawn into the myocardial segments model defined by the American Heart Association (AHA) [46] with 6 segments in the basal and middle slices and 4 segments in the apical slice using the arrayShow [47] tool in MATLAB (MathWorks, Natick, MA). The mean  $T_1$  values were calculated for each segment across all subjects and scans, and were visualized with bulls-eye plots. The repeatability error was calculated using  $\sqrt{(\sum_{i=1}^{n_s} T_{1\text{diff}}^2(i))/n_s}$ , with  $T_{1\text{diff}}(i)$  the  $T_1$  difference between two repeated measurements and  $n_s$  the number of subjects. The precision of  $T_1$  estimation was computed using the coefficient of variation ( $\text{CoV} = \text{SD}_{\text{ROI}} / \text{Mean}_{\text{ROI}} \times 100\%$ ). Further, Bland-Altman analyses were performed to compare ROI-based mean  $T_1$  values between different  $T_1$  mapping techniques. The two-tailed Student’s t-tests were utilized for comparison, and a  $p$  value  $\leq 0.05$  was considered significant. In addition, to quantify the in-plane cardiac motion between end-diastolic and end-systolic phases, the relative difference of the left-ventricular area ( $\text{Area}_{\text{End-Diastolic}} - \text{Area}_{\text{End-Systolic}} / \text{Area}_{\text{End-Diastolic}} \times 100\%$ ), similar to the left-ventricular ejection fraction (LVEF) index for the volume case, was calculated based on the mid-ventricular myocardial  $T_1$  maps. The blood-myocardium boundary was manually segmented using the aforementioned arrayShow tool in MATLAB.

## 4 Results

### Phantom Validation

We first validated the proposed  $T_1$  correction procedure for phantom  $T_1$  mapping when using different delay times in the multi-shot acquisition in comparison to an IR spin-echo reference. Figure 2 presents the estimated  $T_1$  maps for acquisitions with a delay time ranging from five seconds to one second (step size one second) when using the conventional Look-Locker formula and the proposed procedure. Prior to  $T_1$  correction, all the physical parameters  $(M_{ss}, M'_0, R_1^*)^T$  were estimated by the single-slice model-based reconstruction [24] using the data from the second inversion, where the initial magnetization is affected by the incomplete recovery. Both quantitative  $T_1$  maps and  $T_1$  values of a ROI in Figure 2 as well as the Bland-Altman plots in the Supporting Information Figure S1 (A) reveal that the conventional Look-Locker correction underestimates  $T_1$ : the less the delay time, the higher the bias. On the other hand, the proposed procedure could achieve good  $T_1$  accuracy regardless of the delay time, but at the expense of increased noise (i.e., lower precision) for short delays and large  $T_1$  times. This is mainly due to the fact that there is less  $T_1$  information

encoded in the data for shorter delays. In the extreme case where there is no delay, it is impossible to recover  $T_1$  (i.e., decouple  $T_1$  and  $B_1^+$  from  $T_1^*$ ) as no explicit  $T_1$  is encoded in the data. According to these results, a delay time of two seconds or three seconds is a good compromise between short acquisition time and good  $T_1$  precision. We choose three seconds for the other acquisitions in this study.

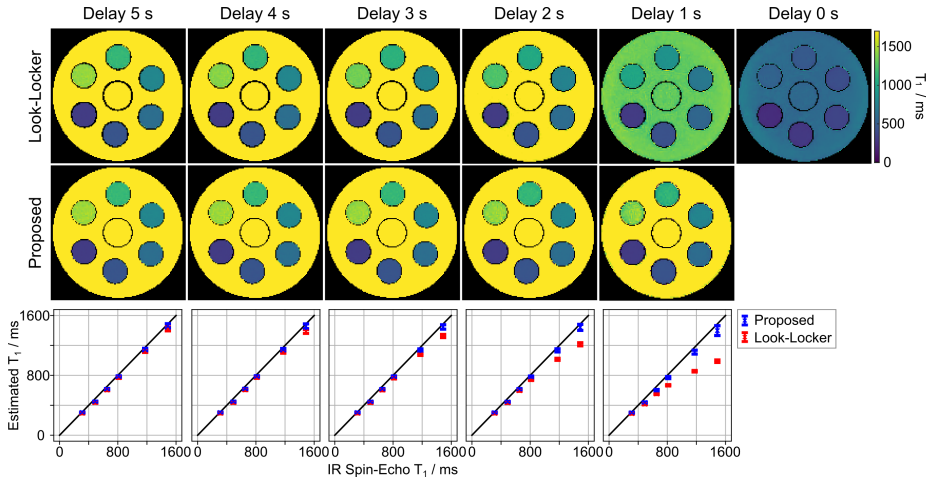


Figure 2: Quantitative phantom  $T_1$  maps with various delay times from 5 s to 1 s (step size 1 s) using (top) the conventional Look-Locker correction and (middle) the proposed formula. (Bottom) Quantitative  $T_1$  values (mean and standard deviation) within ROIs of the 6 phantom tubes in comparison to an IR spin-echo reference. The corresponding Bland-Altman plots are shown in the Supporting Information Figure S1 (A).

Subsequently, we evaluated the proposed motion-resolved model-based reconstruction on the same phantom using the multi-shot data with the delay time of three seconds. The data has been sorted into 6 respiratory and 20 cardiac motion states based on the motion signals estimated from one human subject (subject #3, scan #1). Figure 3 (top) shows the estimated phantom  $T_1$  maps (selected at the end-expiration and end-diastolic phase) with the spatial-only regularization using two different regularization parameters  $\alpha_{\min} = 0.005$  and  $\alpha_{\min} = 0.02$ , and its combination with the spatio-temporal TV regularization with  $\alpha_{\min} = 0.005$ . Figure 3 (bottom) plots the corresponding quantitative  $T_1$  values of the ROI against the IR spin-echo reference. The Supporting Information Figure S1 (B) further presents the corresponding Bland-Altman plots. The above quantitative results show that all reconstructions could achieve a good  $T_1$  accuracy. The increase of the regularization strength in the spatial-only regularization or the use of an additional spatio-temporal TV with the same regularization parameter is helpful for reducing noise (improving  $T_1$  precision)

in the quantitative phantom  $T_1$  maps.

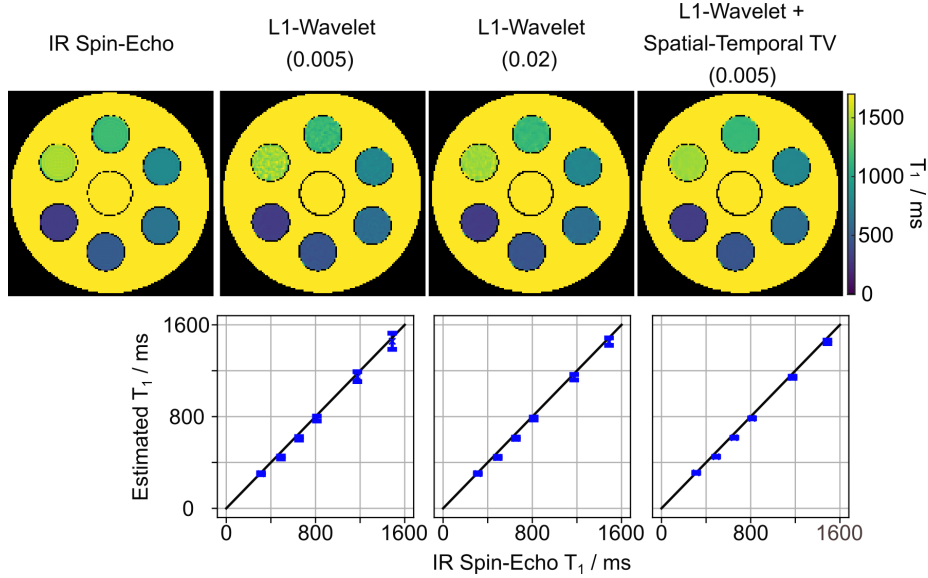


Figure 3: (Top) Phantom  $T_1$  maps reconstructed with different regularization using the motion-resolved model-based reconstruction in comparison to an IR spin-echo reference. (Bottom) Quantitative  $T_1$  values (mean and standard deviation) within ROIs of the 6 phantom tubes. The value in the bracket (top) indicates the regularization parameter  $\alpha_{\min}$  used for each reconstruction. The corresponding Bland-Altman plots are presented in the Supporting Information Figure S1 (B).

## In Vivo Studies

### Respiratory Motion Estimation

Figure 4 shows the DC component for one inversion recovery before and after data correction using the extended orthogonal projection with the order of harmonics  $N_H$  set to be five. Some coils exhibit strong oscillations. The oscillation period in the AC data is linked to the period of the projection angle used in the radial acquisition [28]. By removing this frequency and the higher-order harmonics, these oscillations can be largely eliminated. The filtered DC component is then used for self-gating.

The background of Figure 5 (A) represents the temporal evolution of a line profile extracted from a real-time image reconstruction [45] of the free-running IR radial FLASH with 12 inversions. The line was placed in the vertical direction of the real-time image series where the diaphragmatic motion can be observed, as demonstrated by the white vertical line in Figure 5 (B). On top of the line

profiles, the estimated respiratory signal and the signal provided by the respiratory belt are plotted. All motion signals have been scaled for better visual comparison. The estimated respiratory signal coincides well with the motion of the diaphragm in the real-time images. The adapted SSA-FARY technique could also provide reliable motion signal in the region where the respiratory belt failed to produce a signal (pointed out by a white arrow). Figure 4 (B) shows the corresponding steady-state images reconstructed with the non-uniform fast Fourier transform (nuFFT) after binning the data into 6 respiratory motion states using the estimated respiration signal. As indicated by the dashed lines, the different inspiration and expiration phases are well resolved. Figure 5 (C) and (D) show a similar comparison for the pig experiment where reliable respiratory signal can be obtained, suggesting robustness of the adapted SSA-FARY technique.

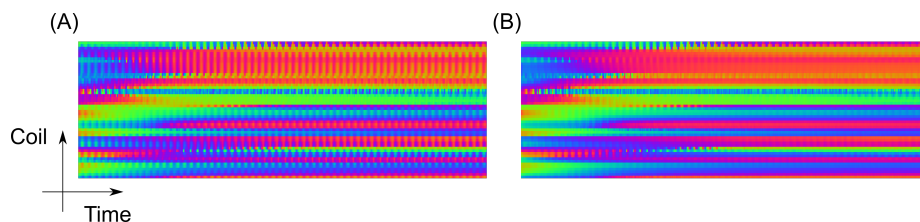


Figure 4: Snippet of the complex plot with color-coded phase of the DC samples used for auto-calibration before (A) and after (B) data correction with the extended orthogonal projection. Notably less disturbing oscillations are observed in B. The above snippet corresponds to one complete inversion recovery (3 s).

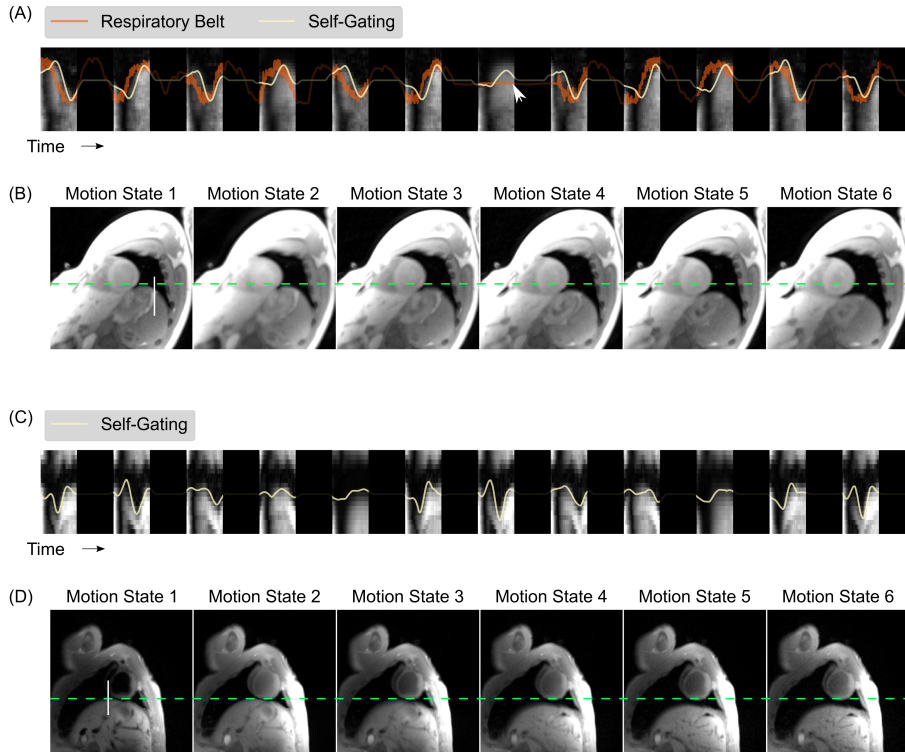


Figure 5: A. Comparison of the estimated respiratory signal with that obtained from the respiratory belt for 12 inversions for a healthy subject. The background image represents the temporal evolution of a vertical line profile (white line in B) extracted from a real-time image reconstruction [45] of the data acquired with free-running IR radial FLASH. The dark regions represent the time delay between inversions. The white arrow indicates a time point where the respiration belt failed to provide a signal. B. The corresponding steady-state images reconstructed by the non-uniform fast Fourier transform after binning the data (combing all cardiac phases) into 6 respiratory motion states. The dashed green line serves as a baseline for the end-respiration motion state. (C) and (D) show similar results for the pig experiment but with the respiratory belt signal absent.

### Model-Based Myocardial $T_1$ Mapping

We validated the effects of different regularization types used in the model-based reconstruction. Figure 6 shows myocardial  $T_1$  maps (at the selected end-expiration and end-diastolic phase) for one subject and the corresponding  $T_1$  line profiles (as indicated by the dashed black line) through all cardiac phases with various regularization types. The regularization parameter  $\alpha_{\min}$  has been opti-

mized for each type of reconstruction individually. In particular,  $\alpha_{\min}$  was set to be 0.02, 0.02, 0.006 and 0.005 for spatial ( $\ell_1$ -Wavelet) only, temporal TV only, combined spatial ( $\ell_1$ -Wavelet) and temporal TV, and the proposed regularization that combines spatial ( $\ell_1$ -Wavelet) and a spatio-temporal TV, respectively. The spatial ( $\ell_1$ -Wavelet) only regularization creates noisy and degraded myocardial  $T_1$  maps. The temporal TV regularization could improve the image quality significantly by exploiting the temporal sparsity. However, this kind of regularization also favors straight lines and thus creates "line"-like artifacts along the time/motion dimension (as seen the line profile images). The combination of spatial ( $\ell_1$ -Wavelet) and temporal TV regularization could reduce these "line"-like effects as a weaker temporal TV regularization is needed to achieve a similar denoising effect. Finally, the spatio-temporal TV regularization that combined both spatial and temporal information in a single multi-dimensional TV regularization, and its combination with the spatial ( $\ell_1$ -Wavelet) regularization, could achieve an even better compromise between denoising and the preservation of subtle motion in the line profiles (indicated by the black arrows) than the other types of regularization. Noteworthy, the myocardial  $T_1$  map from the spatial-only regularization is noisier than our previous single-shot results [27]. This is mainly due to the fact that there is much less data in one motion state in the motion-resolved reconstruction than the one in [27] which combines data from several diastolic phases (e.g.,  $\sim 285$  spokes vs  $\sim 800$  spokes). The Supporting Information Figure S2 shows a similar comparison of the effects of various regularization types on a simulated dynamic phantom with three small tubes on the "myocardium", mimicking certain "lesions". Here, all reconstructions were done with the same regularization parameter. In line with the in vivo results presented here, the spatial regularization-only reconstruction results in blurred images with artifacts and signal inhomogeneities on the "myocardium" due to high undersampling. The temporal TV regularization is able to largely remove the above artifacts and improve image sharpness by exploiting the temporal sparsity but favors "line"-like artifacts along the motion dimension. On the contrary, the proposed spatio-temporal TV combined with the spatial ( $\ell_1$ -Wavelet) regularization has the best performance in denoising and preservation of both spatial and temporal structure details.

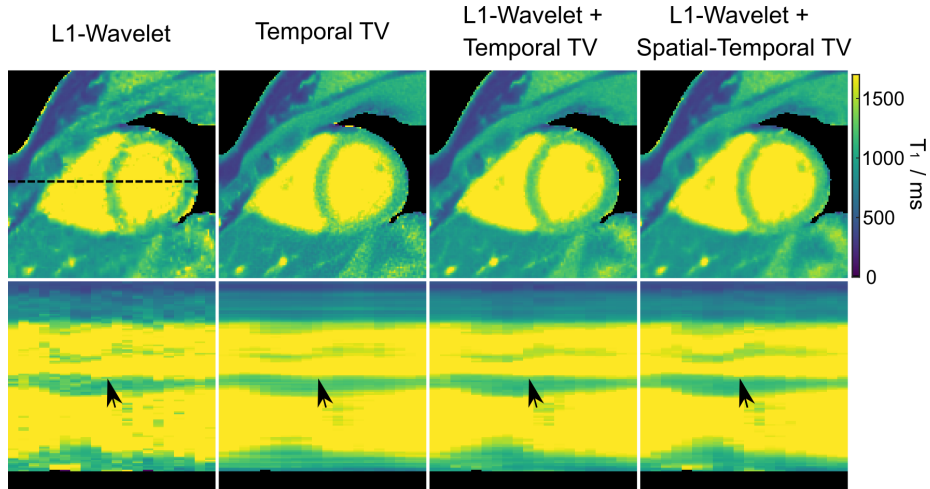


Figure 6: (Top) Myocardial  $T_1$  maps (end-expiration and end-diastolic) with different types of regularization using the proposed motion-resolved model-based reconstruction. (Bottom) Horizontal profiles (dashed black line in the top) through all cardiac phases. The black arrows indicate subtle wall motion that is preserved best with the spatio-temporal TV regularization. Note that the regularization parameter  $\alpha_{\min}$  for each regularization type was tuned individually to achieve a fair comparison.

Figure 7(A) shows the effects of the minimum regularization parameter  $\alpha_{\min}$  on myocardial  $T_1$  maps and the line profiles through the cardiac phases using the combination of the spatio-temporal TV and the spatial ( $\ell_1$ -Wavelet) regularization. Figure 7 (B) presents the corresponding quantitative myocardial septal  $T_1$  values for the ROI. As expected, both qualitative and quantitative results reveal that low values of  $\alpha_{\min}$  result in noisy maps (higher standard deviation) while high values may introduce blurring in the images.  $\alpha_{\min} = 0.005$  was then chosen to balance noise reduction and preservation of anatomical details.

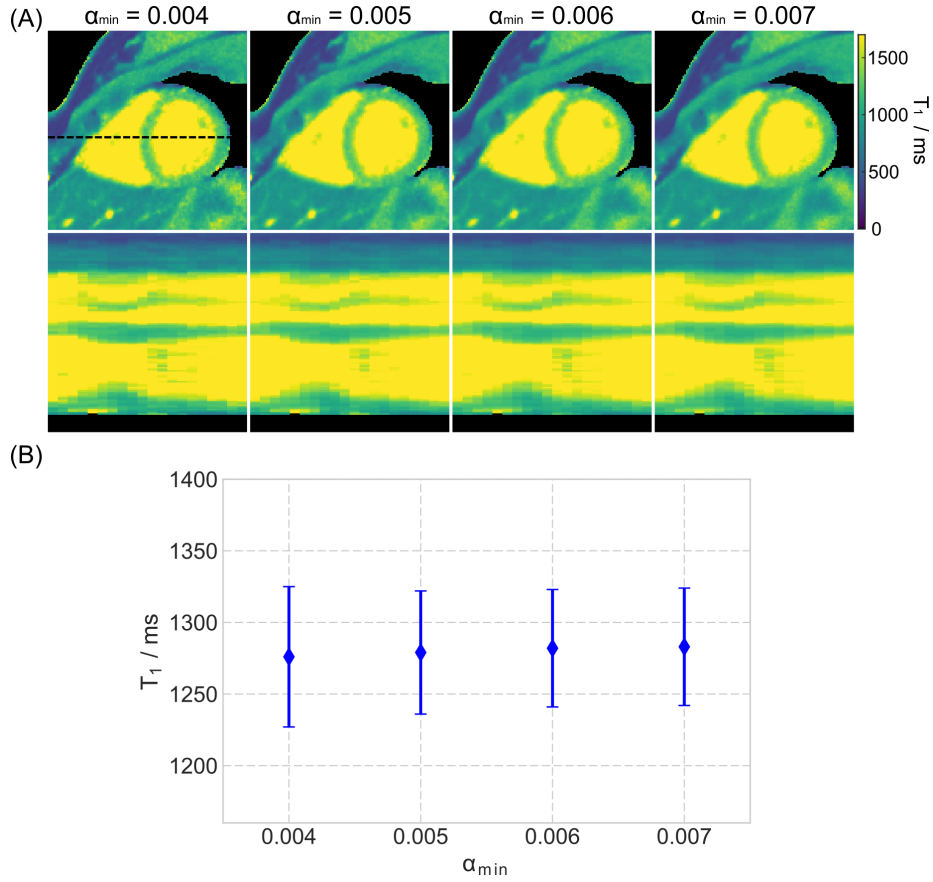


Figure 7: A. (Top) Myocardial  $T_1$  maps (end-expiration and end-diastolic) estimated with motion-resolved model-based reconstruction with different choices of the minimum regularization parameter  $\alpha_{\min}$ . (Bottom) Horizontal profiles (dashed black line in the top) through all cardiac phases. B. Quantitative  $T_1$  values (mean and standard deviation) within a ROI in the septal region.

With the above settings, Figure 8 shows a MOLLI  $T_1$  map and two mid-ventricular myocardial  $T_1$  maps at the end-diastolic and end-systolic phases (the same respiratory motion state) as well as the  $T_1$  line profile through the cardiac phase using the proposed method for two representative subjects. Although the breathing conditions are different, diastolic myocardial  $T_1$  maps are visually comparable between MOLLI and the free-breathing technique. Besides the diastolic  $T_1$  map, the proposed method could also provide myocardial  $T_1$  maps at other cardiac phases.

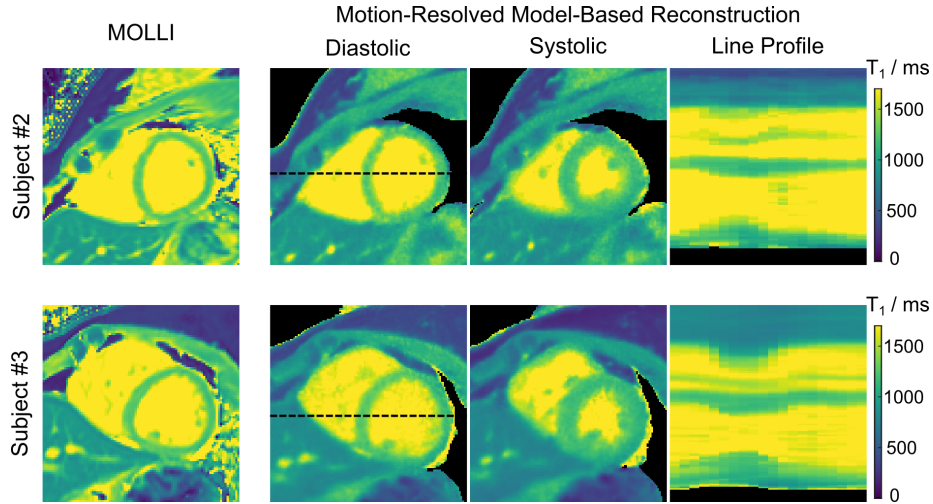


Figure 8: Diastolic and systolic myocardial  $T_1$  maps (end-expiration) and line profiles through the cardiac phase of the motion-resolved model-based reconstruction acquired during free breathing in comparison to MOLLI acquired in a breathhold for two representative subjects.

The Supporting Information Figure S3 then presents two repetitive mid-ventricular myocardial  $T_1$  maps (end-expiration and end-diastolic) of the proposed method and a MOLLI  $T_1$  map for all subjects. Despite differences in breathing conditions between scans, the free-breathing  $T_1$  maps are visually comparable between the two repetitive scans for all subjects. Figure 9 (A) shows the Bullseye plots of quantitative  $T_1$  values and measurement repeatability errors for the six mid-ventricular segments of all subjects and scans for both the proposed motion-resolved model-based reconstruction and MOLLI techniques. Figure 9 (B) compares diastolic  $T_1$  values for all the mid-ventricular segments and the septal segments (segments 8 and 9 according to AHA) for both methods. The paired t-test comparison for each segment are summarized in the Supporting Information Table S3. The above quantitative comparison demonstrates that the proposed technique has slightly shorter mean  $T_1$  values for all segments ( $1218 \pm 57$  ms vs  $1231 \pm 40$  ms) but longer  $T_1$  values for the septum segments ( $1261 \pm 35$  ms vs  $1250 \pm 28$  ms) than MOLLI. However, no significant differences were found in most of the AHA segments, except for the lateral segments where MOLLI has longer  $T_1$  values. Noteworthy, all the above  $T_1$  values are within the published normal range at 3T [48]. Moreover, the proposed method has a slightly lower  $T_1$  precision (higher CoV values) than MOLLI (CoV:  $4.7\% \pm 1.6\%$  vs  $2.8\% \pm 1.1\%$ ,  $p < 0.01$ ) but are comparable to MOLLI in the repeatability errors ( $38 \pm 17$  ms vs  $31 \pm 13$  ms,  $p = 0.47$ ) for all mid-ventricular segments. The Bland-Altman plot in the Supporting Information Figure S4 further reveal that the proposed  $T_1$  correction formula generates longer  $T_1$  values than the

conventional Look-Locker correction technique ( $1261 \pm 35$  ms vs  $1233 \pm 29$  ms,  $p < 0.01$ ).

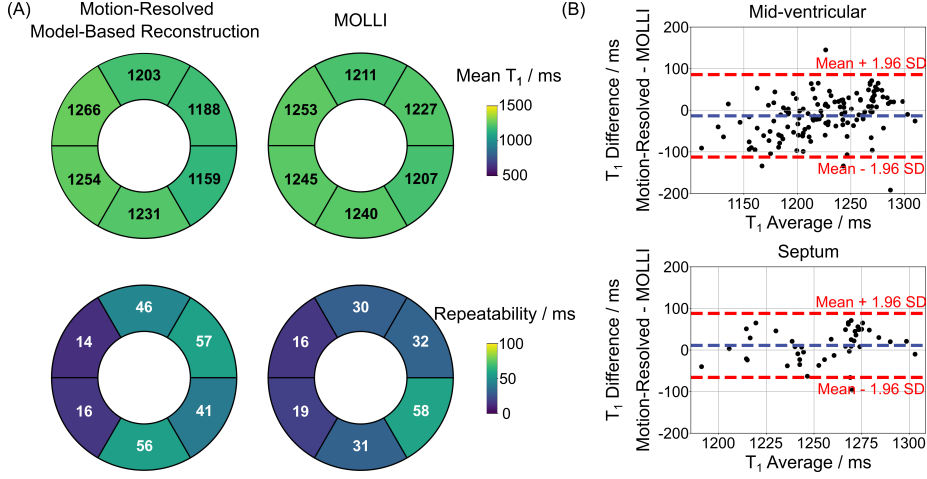


Figure 9: A. Bullseye plots of six mid-ventricular myocardial segments, showing (top) the mean diastolic  $T_1$  values and (bottom) the measurement repeatability errors for all eleven subjects and all scans for (left) the motion-resolved model-based reconstruction (free-breathing) and (right) the MOLLI method (breath-hold), respectively. B. Bland–Altman plots comparing the mean diastolic  $T_1$  values of (top) all the six mid-ventricular segments (mean difference: -13 ms, SD: 51 ms) and (bottom) the septal segments (segments 8 and 9 according to AHA, mean difference: 11 ms, SD: 39 ms) for the proposed method and MOLLI for all subjects and scans.

Representative basal and apical diastolic myocardial  $T_1$  maps, in addition to the mid-slice  $T_1$  map, from two subjects, are shown in the Supporting Information Figure S5 (A). Quantitative results from both basal and apical slices and their comparison to MOLLI are presented in the Supporting Information Figure S5 (B) and (C). Again, although slight mean  $T_1$  difference is observed between the motion-resolved model-based reconstruction and MOLLI techniques, no significant differences were found in all the basal and apical AHA segments as shown in the Supporting Information Table S3. The Supporting Information Table S4 further shows the relative difference of the left-ventricular area calculated from the myocardial  $T_1$  maps. We observe good repeatability (repeatability error: 3%) between scans. Although the results are obtained from a single slice, they are generally in the expected range for LVEF values. In addition, the quantitative  $T_1$  maps and ROI-analyzed  $T_1$  values in the Supporting Information Figure S6 demonstrate good agreements between the proposed approach and MOLLI for the pig experiment, i.e., both methods show higher and similar myocardial  $T_1$  values in the infarcted septal and anterior wall regions,

suggesting robustness of the proposed approach.

Aside from quantitative myocardial  $T_1$  maps, Figure 10 presents synthesized  $T_1$ -weighted cardiac images (bright blood and dark blood) at the two cardiac phases for the same subjects shown in Figure 8. Both the bright-blood and dark-blood-weighted images clearly resolve the contrast between myocardium and blood pool. The synthetic images and myocardial  $T_1$  maps at all cardiac phases were then converted into movies which are available as Supporting Information Videos S1 and S2. Similarly, a synthetic image series for all inversion times and all cardiac phases of one subject can be found in the Supporting Information Video S3.

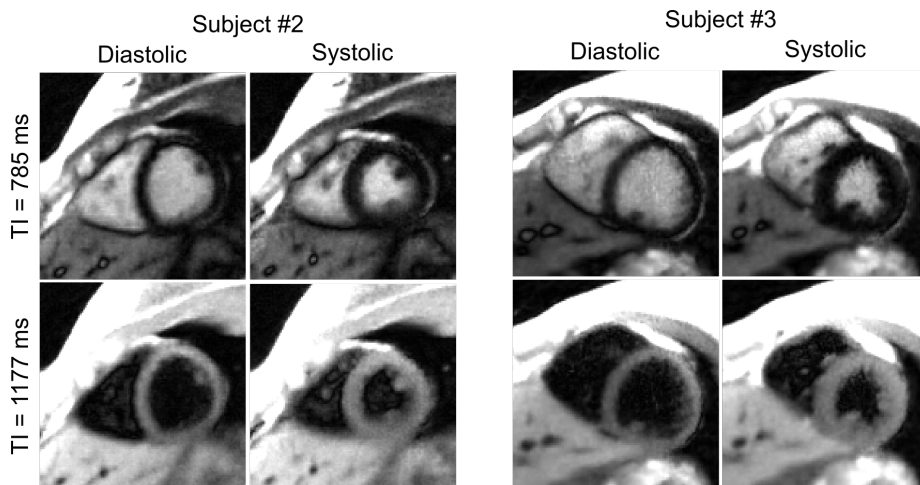


Figure 10: Synthesized  $T_1$ -weighted images at two representative inversion times (bright blood and dark blood) for the end-diastolic and end-systolic cardiac phases for the same subjects shown in Figure 8.

## 5 Discussion

In this work, we have developed a free-breathing high-resolution myocardial  $T_1$  mapping technique using a free-running inversion-recovery radial FLASH sequence and a calibrationless motion-resolved model-based reconstruction. Instead of continuous acquisitions, we adopt a delay time between inversions to encode  $T_1$  information and have derived a correction procedure for accurate  $T_1$  estimation without the need of full  $T_1$  recovery or additional  $B_1^+$  mapping. We further adapted the SSA-FARY strategy for robust respiratory motion signal estimation from the zero-padded AC region where the trajectory-dependent oscillations and contrast changing signal (due to inversion) have been eliminated in preprocessing. Following self-gating and data sorting, we propose to estimate both parameter maps and coil sensitivity maps of the desired motion states di-

rectly from k-space using an extended motion-resolved model-based reconstruction. The latter avoids any coil calibration and can employ high-dimensional spatio-temporal TV regularization, in addition to the spatial regularization, to improve precision in  $T_1$  while preserving the spatio-temporal information. Studies have been performed on an experimental phantom, eleven healthy subjects and one young landrace pig with infarcted myocardium.

The phantom results demonstrate good  $T_1$  accuracy of the proposed approach over a wide range of  $T_1$  times. In vivo studies have shown similar diastolic myocardial  $T_1$  values between the proposed approach and MOLLI for all segments, except for the lateral segments. The  $T_1$  difference in the lateral regions between the two approaches and the difference between lateral and septal  $T_1$  values can also be seen in other  $T_1$  mapping techniques, such as MR multitasking [15] and ref.[26]. The origin of these differences is not clear: They could be caused by residual myocardial motion in the lateral regions, which makes the lateral segments violate the assumed signal model, by partial volume effects with the surrounding pericardium, or by difficulties in selecting the diastolic ROIs in the thin myocardium [26]. While  $T_1$  values of the proposed approach correspond well with MOLLI, the proposed approach may still underestimate  $T_1$  due to the imperfect inversion caused by the non-selective hyperbolic secant pulse we used. Although a scaling factor (reciprocal of the inversion efficiency,  $> 1$ ) can be employed in the post-processing step to compensate such an imperfection [49], we would rather acknowledge such a limitation in this work and investigate this issue by designing a more efficient inversion pulse in our further study. The precision of the proposed method (CoV:  $4.7\% \pm 1.6\%$ ) is lower than that of MOLLI (CoV:  $2.8\% \pm 1.1\%$ ). Such a difference could be explained by the differences in the nominal spatial resolution (MOLLI:  $1.4 \times 1.4 \times 8 \text{ mm}^3$ , the proposed:  $1.0 \times 1.0 \times 6.0 \text{ mm}^3$ ) and the readouts (MOLLI: Cartesian balanced SSFP, the proposed: radial FLASH). Nevertheless, the proposed approach shows comparable (CoV: 4.9% with  $1.3 \times 1.3 \times 8 \text{ mm}^3$  in ref. [26], CoV: 4.8% with  $1.7 \times 1.7 \times 8 \text{ mm}^3$  in MR multitasking [15]) or even slightly better (CoV: 5.7% with  $1.6 \times 1.6 \times 8 \text{ mm}^3$  in MRF [11])  $T_1$  precision when comparing to other well-known techniques.

Continuous acquisitions with constant flip angles [16, 17] have been used in several inversion-prepared free-running  $T_1$  mapping techniques attributed to the scan efficiency. I.e., there is no waiting time between inversions. However, as pointed out by [19], continuous acquisition with the same flip angle only encodes  $T_1^*$  information in the data [32]. Since  $T_1^*$  is a function of flip angle and  $T_1$ , additional information about  $B_1^+$  is therefore necessary for accurate  $T_1$  estimation. However, the additional estimation of  $B_1^+$  at the same motion state might be difficult to achieve in free-breathing, self-gated acquisitions. In [19], Zhou et al. propose to solve this issue by introducing a dual flip-angle strategy which acquires data continuously with two flip angles consecutively applied. Following self-gated data sorting, image reconstruction and dictionary matching, two different  $T_1^*$  maps from the same motion state can be extracted and subsequently be used to calculate both  $T_1$  and  $B_1^+$  maps in an iterative manner. Most recently, a similar idea has been proposed in the MR multitasking

technique for more accurate  $T_1$  mapping [50]. Alternatively, in this work, we propose to resolve this problem by adopting a delay time between inversions, using this period for encoding  $T_1$  information in the data. Different from studies which set the delay time long enough to ensure a full recovery of longitudinal magnetization, we are capable of estimating accurate  $T_1$  even with an incomplete  $T_1$  recovery, shortening the acquisition time. Moreover, the proposed approach requires neither additional  $B_1^+$  mapping nor the explicit calculation of  $B_1^+$  from the data.

Self-gating constitutes another key component for free-breathing imaging. Although a few self-gating techniques have been successfully developed for steady-state imaging, estimation of reliable motion signals from the contrast-modulated k-space is challenging. In this work, following removal of signal oscillations in the k-space center signal, we model the additive and multiplicative effects caused by inversion in the data following [35] and propose to reduce such effects prior to the application of the SSA-FARY-based self-gating techniques. From our experience, the above step is crucial for reliable motion estimation using SSA-FARY. Although the proposed method could achieve robust respiration signal estimation, the determination of reliable cardiac signals from the filtered k-space remained challenging and retrospective ECG gating was used for binning. Resolving the latter issue in a future work would be of value as the ECG signal is not always reliable [34], which we also observed for several data sets acquired for this study.

Inspired by the high-dimensional imaging techniques [37, 51, 52, 15, 53], we have sorted the data into multiple cardiac and respiratory motion states, and applied high-dimensional regularization along these motion dimensions to improve  $T_1$  accuracy and precision. In contrast, several other studies [17, 19] combined data from multiple respiratory motion states into one using rigid image registration, following respiratory motion field being estimated from low-resolution images. The latter strategy has the advantage that more data is available for each cardiac phase than the one that sorts the data into multiple respiratory and cardiac motion states within the same amount of time. However, as motion between respiratory states is usually considered to be nonlinear [54] for cardiac imaging, a linear model may cause data mismatch in the cost function, resulting in reconstruction errors. Most recently, advanced nonlinear motion estimation methods have been developed for whole-heart coronary MR imaging [55]. Integration of such a nonlinear motion model into the model-based reconstruction framework would also be of great interest as it has the potential to shorten the total acquisition time of the proposed method while preserving good  $T_1$  accuracy and precision.

Spatio-Temporal regularization has been shown to be more effective in exploiting sparsity in compressed-sensing reconstructions for dynamic/high-dimensional imaging, resulting in higher acceleration factors than the spatial regularization-only reconstruction [37, 51, 15]. This work confirms the above findings in the regularized nonlinear model-based reconstruction for dynamic myocardial  $T_1$  mapping. Moreover, our results demonstrate that the spatio-temporal TV regularization has a slightly better performance in both image denoising and preser-

vation of structure details than the temporal TV regularization. On the other hand, although the regularization used in this study is effective in reducing noise/improving quantitative precision, it may also cause a certain degree of image blurring (lower effective spatial resolution) similar to other regularization techniques used in compressed sensing. More advanced regularization, such as neural network-enhanced regularizers [56] could be employed in future studies to solve the above issue.

The proposed method takes around two minutes for reliable  $T_1$  estimation, which compares well to alternative techniques when considering the relatively high nominal resolution of the  $T_1$  maps ( $1.0 \times 1.0 \times 6 \text{ mm}^3$ ). The acquisition time could be shorted by further reducing the delay time. Here, we adopted the three-second delay to achieve a good compromise of  $T_1$  accuracy and precision. However, in principle, a delay time of one second could be used (at a cost of lower precision), resulting in an acquisition time of around 80 s.

There are also other limitations of the present work need to be mentioned. First, the blood  $T_1$  estimated by methods using continuous acquisition may not be reliable as the in-flow effects make the blood violate the assumed signal model, a problem which also affects other methods based on continuous acquisition [57, 19, 17]. Thus, the proposed method is not ideal for estimating the extracellular volume (ECV). However, as pointed out by [17], when ECV is needed, blood  $T_1$  values could be calculated from a rapid low-resolution (enough to define a blood ROI) free-breathing blood  $T_1$  mapping sequence in the mid-ventricular slice. Second, evaluation of the proposed method has so far only been done in healthy volunteers. Validation of the proposed free-breathing method in patient studies with both native and post-contrast  $T_1$  mapping is now warranted and will be the subject of future work. Another limitation of the proposed method is the long computation time. Although substantial efforts have been made in the implementation part to enable model-based reconstruction to run on GPUs, which already reduced reconstruction time from several hours to 25 minutes, further efforts are still needed to reduce computation time.

## 6 Conclusion

The proposed free-breathing method enables high-resolution  $T_1$  mapping with good  $T_1$  accuracy, precision and repeatability by combing inversion-recovery radial FLASH, self-gating and a calibrationless motion-resolved model-based reconstruction.

## 7 Acknowledgement

We thank Dr. Haikun Qi from ShanghaiTech University for insightful discussions.

## A Appendix

### Appendix I: Oscillation Removal

As described in [28], for the steady-state AC signal  $\mathbf{X}$ , we want to remove an oscillation which can be described by the basis:

$$\mathbf{n}^t = \begin{pmatrix} e^{+i\psi_0 \cdot t} \\ e^{-i\psi_0 \cdot t} \\ e^{+2i\psi_0 \cdot t} \\ e^{-2i\psi_0 \cdot t} \\ \vdots \\ e^{+N_H i\psi_0 \cdot t} \\ e^{-N_H i\psi_0 \cdot t} \end{pmatrix},$$

with  $\psi_0 \cdot t$  the projection angle at time  $t$ ,  $\psi_0$  the incremental projection angle and  $N_H$  the highest order of the harmonic in the basis. Therefore, the corrected signal is  $\mathbf{X}_{\text{cor}} = \mathbf{X} - \mathbf{n}(\mathbf{n}^\dagger \mathbf{X})$  with  $^\dagger$  denoting the pseudo-inverse.  $\mathbf{n}(\mathbf{n}^\dagger \mathbf{X})$  is the projection of  $\mathbf{X}$  onto the basis  $\mathbf{n}$ .

For inversion prepared acquisitions, the contrast changes along time. The new centered k-space signal  $\tilde{\mathbf{X}}$  can then be modeled by a global modulation for each channel  $c$ , i.e.,  $\tilde{X}_c(t) = \phi_c(t)X_c(t)$ , where  $\phi_c(t)$  describes the contrast change, and  $\tilde{X}_c(t)$ ,  $X_c(t)$  are the  $c$ th components of  $\tilde{\mathbf{X}}$  and  $\mathbf{X}$ , respectively. As  $X_c(t) = \sum_i n_i w_i + \eta$  with  $w_i$  the weighting factor and  $\eta$  the noise [28],  $\tilde{X}_c(t) = \phi_c(t)X_c(t) = \sum_i \phi_c(t)n_i w_i + \phi_c(t)\eta$ . Thus, our new basis for each channel becomes:

$$\tilde{\mathbf{n}}_c = \phi_c(t) \cdot \mathbf{n}_c$$

$\phi_c(t)$  can be determined using a moving average filter:  $\phi_c(t) = \text{movavg}(\tilde{X}_c(t))$ . The newly corrected signal is then:  $\tilde{\mathbf{X}}_{\text{cor}} = \tilde{\mathbf{X}} - \tilde{\mathbf{n}}(\tilde{\mathbf{n}}^\dagger \tilde{\mathbf{X}})$ .

## Appendix II: IRGNM-ADMM algorithm

**OUTPUTS:**  $(M_{ss}, M'_0, R_1^*)^T$  and  $(c_1, \dots, c_{N_C})^T$  for all motion states

**INPUTS:**

$Y \leftarrow$  Gridded and sorted k-space data;

$P \leftarrow$  Sampling pattern;

$(t_1, \dots, t_{n_{TI}})^T \leftarrow$  Vector of inversion times for each motion state;

% Initialization for IRGNM:

$n = 0, \alpha_0 = \beta_0 = 1, \text{MaxIter} = 10, x_0 = (1, 1, 1.5, 0, \dots, 0)^T$

% Define  $A$  to be the block diagonal matrix with the blocks  $A_{r,c}$  on the diagonal and

%  $b$  the stacked vector of  $b_{r,c}$  where

$$\begin{aligned} A_{r,c} &= DF_{r,c}(x_n) \\ b_{r,c} &= DF_{r,c}(x_n)x_n - F_{r,c}(x_n) + Y_{r,c} \end{aligned}$$

% Gauss-Newton Iterations:

**while**  $n < \text{MaxIter}$  **do**

    % Solve the following subproblem with ADMM:

    %  $x_{n+1} = \arg \min_{x \in S} \|Ax - b\|_2^2 + \alpha_n R(x_m) + \beta_n U(x_c)$ ,  
    with  $x = (x_m, x_c)^T$ .

    % Initialization for ADMM:

$k = 0, K = \min(100, 10 \cdot 2^n), \rho = 0.01, z^k = y^k = x_n$ .

    % ADMM Iterations:

**for**  $k < K$  **do**

$x^{k+1} \leftarrow (A^H A + \rho I)^{-1} (A^H b + \rho z^k - y^k)$

        % solved by conjugate gradient;

$z_m^{k+1} \leftarrow \text{prox}_{\alpha_n/\rho}^m(x_m^{k+1} + y_m^k/\rho)$

        % proximal operators for parameter maps  $x_m$ ;

$z_c^{k+1} \leftarrow \text{prox}_{\beta_n/\rho}^c(x_c^{k+1} + y_c^k/\rho)$

        % proximal operators for coil sensitivity maps  $x_c$ ;

$y^{k+1} \leftarrow y^k + \rho(x^{k+1} - z^{k+1})$ ;

**end**

$x_{n+1} = y^{k+1}$ ;

$\alpha_{n+1} = \max(\alpha_{\min}, (\frac{1}{3})^n \cdot \alpha_0)$ ;

$\beta_{n+1} = (\frac{1}{3})^n \cdot \beta_0$ ;

$n = n + 1$ ;

**end**

### Algorithm 1: IRGNM-ADMM algorithm

In the above algorithm,  $\text{prox}_{\alpha_n/\rho}^m$  contains the following three proximal operators:

$Z_m^{k+1} := W^H S_{\alpha_n/\rho}(W Z_m^k)$  (Wavelet-domain joint soft-thresholding)

$Z_m^{k+1} := P_S(Z_m^k)$  (projection of  $Z_m^k$  onto domain  $S$ )

$Z_m^{k+1} := D^H S_{\alpha_n/\rho} D Z_m^k$  (Total variation gradient-domain soft-thresholding)

and  $\text{prox}_{\alpha_n/\rho}^c$  is the least-square proximal operator, i.e.,

$$Z_c^{k+1} := \frac{1}{2}Z_c^k.$$

### Appendix III: Memory-efficient GPU Implementation

In general, the numerical optimization requires a huge amount of memory, involving the storage of the gridded k-space  $Y$ , the derivatives  $DF$ , and temporary memory to hold intermediate results in during the computation of  $F$  and  $DF$ . The gridded k-space  $Y$  and correspondingly  $b$  require the most memory. Both have dimensions  $(2N_x) \times (2N_y) \times N_C \times N_S \times T_C \times T_R$ . With a typical problem size of  $640 \times 640 \times 6 \times 27 \times 20 \times 3$  single precision complex float numbers, this corresponds to a memory of around 32GB. In contrast, the derivatives  $DF_{r,c}$  require about 10GB, the variables in the parameter space  $(x, y, z)$  require about 2GB each and the temporary variables to compute the proximal operators require about 25GB in total. To optimally utilize the available GPU-memory, we store the large variables  $Y$  and  $b$  in CPU-memory. The linear subproblem is solved completely on the GPU, however, all computations involving  $F$ ,  $DF$  and  $A^H A$  are performed independently and sequentially for the different motion states on the GPU. Thus, the complete gridded k-space does not need to be stored simultaneously on the GPU, as it would be the case if  $A^H A$  was computed jointly for all motion states. With the above strategies, we are able to reduce the required GPU memory to about 70GB, making the model-based reconstruction feasible on a single NVIDIA A100 GPU with 80GB memory. Compared to a CPU (40-core 2.3 GHz Intel Xeon E5-2650 server with a RAM size of 512 GB) reconstruction, this strategy reduces the computational time from 12 hours to around 25 minutes. Moreover, the block-wise computation of  $F$  and  $DF$  enables the distribution of the computations to multiple GPUs, allowing for further accelerations. For example, with a two-GPU system, the memory required on the first GPU reduces to about 60GB and the reconstruction time can be reduced to about 15 minutes per dataset. Note that the required memory is not halved by using two GPUs since the computation of the proximal operators cannot be distributed.

### References

- [1] Moon JC, Messroghli DR, Kellman P, Piechnik SK, Robson MD, Ugander M, Gatehouse PD, Arai AE, Friedrich MG, Neubauer S et al. Myocardial T1 mapping and extracellular volume quantification: a Society for Cardiovascular Magnetic Resonance (SCMR) and CMR Working Group of the European Society of Cardiology consensus statement. *J. Cardiovasc. Magn. Reson.* 2013; 15:92.
- [2] Kellman P, Hansen MS. T1-mapping in the heart: accuracy and precision. *J. Cardiovasc. Magn. Reson.* 2014; 16:2.

- [3] Puntmann VO, Voigt T, Chen Z, Mayr M, Karim R, Rhode K, Pastor A, CarrWhite G, Razavi R, Schaeffter T et al. Native T1 mapping in differentiation of normal myocardium from diffuse disease in hypertrophic and dilated cardiomyopathy. *JACC: Cardiovascular Imaging* 2013; 6:475–484.
- [4] Messroghli DR, Radjenovic A, Kozerke S, Higgins DM, Sivananthan MU, Ridgway JP. Modified Look-Locker Inversion recovery (MOLLI) for high-resolution T1 mapping of the heart. *Magn. Reson. Med.* 2004; 52:141–146.
- [5] Chow K, Flewitt JA, Green JD, Pagano JJ, Friedrich MG, Thompson RB. Saturation recovery single-shot acquisition (SASHA) for myocardial T1 mapping. *Magn. Reson. Med.* 2014; 71:2082–2095.
- [6] Weingärtner S, Akçakaya M, Basha T, Kissinger KV, Goddu B, Berg S, Manning WJ, Nezafat R. Combined saturation/inversion recovery sequences for improved evaluation of scar and diffuse fibrosis in patients with arrhythmia or heart rate variability. *Magn. Reson. Med.* 2014; 71:1024–1034.
- [7] Piechnik SK, Ferreira VM, Dall’Armellina E, Cochlin LE, Greiser A, Neubauer S, Robson MD. Shortened Modified Look-Locker Inversion recovery (ShMOLLI) for clinical myocardial T1-mapping at 1.5 and 3 T within a 9 heartbeat breathhold. *J. Cardiovasc. Magn. Reson.* 2010; 12:1.
- [8] Gensler D, Mörchel P, Fidler F, Ritter O, Quick HH, Ladd ME, Bauer WR, Ertl G, Jakob PM, Nordbeck P. Myocardial T1 quantification by using an ECG-triggered radial single-shot inversion-recovery MR imaging sequence. *Radiology* 2014; 274:879–887.
- [9] Wang X, Joseph AA, Kalentev O, Merboldt KD, Voit D, Roeloffs VB, van Zalk M, Frahm J. High-resolution myocardial T1 mapping using single-shot inversion recovery fast low-angle shot MRI with radial undersampling and iterative reconstruction. *Brit. J. Radiol.* 2016; 89:20160255.
- [10] Marty B, Coppa B, Carlier PG. Fast, precise, and accurate myocardial T1 mapping using a radial MOLLI sequence with FLASH readout. *Magn. Reson. Med.* 2018; 79:1387–1398.
- [11] Hamilton JI, Jiang Y, Chen Y, Ma D, Lo WC, Griswold M, Seiberlich N. MR fingerprinting for rapid quantification of myocardial T1, T2, and proton spin density. *Magn. Reson. Med.* 2017; 77:1446–1458.
- [12] Jaubert O, Cruz G, Bustin A, Hajhosseiny R, Nazir S, Schneider T, Koken P, Doneva M, Rueckert D, Masci PG et al. T1, T2, and fat fraction cardiac MR fingerprinting: preliminary clinical evaluation. *J. Magn. Reson. Imaging* 2021; 53:1253–1265.
- [13] Liu Y, Hamilton J, Eck B, Griswold M, Seiberlich N. Myocardial T1 and T2 quantification and water–fat separation using cardiac MR fingerprinting

with rosette trajectories at 3T and 1.5 T. *Magnetic Resonance in Medicine* 2021; 85:103–119.

- [14] Lima da Cruz GJ, Velasco C, Lavin B, Jaubert O, Botnar RM, Prieto C. Myocardial T1, T2, T2\*, and fat fraction quantification via low-rank motion-corrected cardiac MR fingerprinting. *Magn. Reson. Med.* 2022; DOI: <https://doi.org/10.1002/mrm.29171>.
- [15] Christodoulou AG, Shaw JL, Nguyen C, Yang Q, Xie Y, Wang N, Li D. Magnetic resonance multitasking for motion-resolved quantitative cardiovascular imaging. *Nat. Biomed. Eng.* 2018; 2:215.
- [16] Shaw JL, Yang Q, Zhou Z, Deng Z, Nguyen C, Li D, Christodoulou AG. Free-breathing, non-ECG, continuous myocardial T1 mapping with cardiovascular magnetic resonance multitasking. *Magn. Reson. Med.* 2019; 81:2450–2463.
- [17] Qi H, Jaubert O, Bustin A, Cruz G, Chen H, Botnar R, Prieto C. Free-running 3D whole heart myocardial T1 mapping with isotropic spatial resolution. *Magn. Reson. Med.* 2019; 82:1331–1342.
- [18] Guo R, Cai X, Kucukseymen S, Rodriguez J, Paskavitz A, Pierce P, Goddu B, Nezafat R. Free-breathing whole-heart multi-slice myocardial T1 mapping in 2 minutes. *Magn. Reson. Med.* 2021; 85:89–102.
- [19] Zhou R, Weller DS, Yang Y, Wang J, Jeelani H, MuglerIII JP, Salerno M. Dual-excitation flip-angle simultaneous cine and T1 mapping using spiral acquisition with respiratory and cardiac self-gating. *Magn. Reson. Med.* 2021; 86:82–96.
- [20] Block KT, Uecker M, Frahm J. Model-Based Iterative Reconstruction for Radial Fast Spin-Echo MRI. *IEEE Trans. Med. Imaging* 2009; 28:1759–1769.
- [21] Fessler JA. Model-based image reconstruction for MRI. *IEEE Signal Process. Mag.* 2010; 27:81–89.
- [22] Wang X, Tan Z, Scholand N, Roeloffs V, Uecker M. Physics-based reconstruction methods for magnetic resonance imaging. *Philos. Trans. R. Soc. A* 2021; 379:20200196.
- [23] Zhao B, Lam F, Liang Z. Model-Based MR Parameter Mapping With Sparsity Constraints: Parameter Estimation and Performance Bounds. *IEEE Trans. Med. Imaging* 2014; 33:1832–1844.
- [24] Wang X, Roeloffs V, Klosowski J, Tan Z, Voit D, Uecker M, Frahm J. Model-based T1 mapping with sparsity constraints using single-shot inversion-recovery radial FLASH. *Magn. Reson. Med.* 2018; 79:730–740.

- [25] Maier O, Schoormans J, Schloegl M, Strijkers GJ, Lesch A, Benkert T, Block T, Coolen BF, Bredies K, Stollberger R. Rapid T1 quantification from high resolution 3D data with model-based reconstruction. *Magn. Reson. Med.* 2019; 81:2072–2089.
- [26] Becker KM, SchulzMenger J, Schaeffter T, Kolbitsch C. Simultaneous high-resolution cardiac T1 mapping and cine imaging using model-based iterative image reconstruction. *Magn. Reson. Med.* 2019; 81:1080–1091.
- [27] Wang X, Kohler F, UnterbergBuchwald C, Lotz J, Frahm J, Uecker M. Model-based myocardial T1 mapping with sparsity constraints using single-shot inversion-recovery radial FLASH cardiovascular magnetic resonance. *J. Cardiovasc. Magn. Reson.* 2019; 21:60.
- [28] Rosenzweig S, Scholand N, Holme HCM, Uecker M. Cardiac and Respiratory Self-Gating in Radial MRI using an Adapted Singular Spectrum Analysis (SSA-FARY). *IEEE Trans. Med. Imaging* 2020; 39:3029–3041.
- [29] Wundrak S, Paul J, Ulrici J, Hell E, Geibel MA, Bernhardt P, Rottbauer W, Rasche V. Golden ratio sparse MRI using tiny golden angles. *Magn. Reson. Med.* 2016; 75:2372–2378.
- [30] Wang X, Rosenzweig S, Scholand N, Holme HCM, Uecker M. Model-based Reconstruction for Simultaneous Multi-slice T1 Mapping using Single-shot Inversion-recovery Radial FLASH. *Magn. Reson. Med.* 2021; 85:1258–1271.
- [31] Feng L, Liu F, Soultanidis G, Liu C, Benkert T, Block KT, Fayad ZA, Yang Y. Magnetization-prepared GRASP MRI for rapid 3D T1 mapping and fat/water-separated T1 mapping. *Magn. Reson. Med.* 2021; 86:97–114.
- [32] Look DC, Locker DR. Time saving in measurement of NMR and EPR relaxation times. *Rev. Sci. Instrum.* 1970; 41:250–251.
- [33] Deichmann R, Haase A. Quantification of T1 values by SNAPSHOT-FLASH NMR imaging. *J. Magn. Reson.* (1969) 1992; 96:608–612.
- [34] Larson AC, White RD, Laub G, McVeigh ER, Li D, Simonetti OP. Self-gated cardiac cine MRI. *Magn. Reson. Med.* 2004; 51:93–102.
- [35] Winter P, Kampf T, Helluy X, Gutjahr FT, Meyer CB, Bauer WR, Jakob PM, Herold V. Self-navigation under non-steady-state conditions: Cardiac and respiratory self-gating of inversion recovery snapshot FLASH acquisitions in mice. *Magn. Reson. Med.* 2016; 76:1887–1894.
- [36] Rosenzweig S, Uecker M. Novel insights on SSA-FARY: Amplitude-based respiratory binning in self-gated cardiac MRI. In: *Proc. Intl. Soc. Mag. Reson. Med., Virtual*, 2021. p. 1956.

- [37] Feng L, Axel L, Chandarana H, Block KT, Sodickson DK, Otazo R. XD-GRASP: Golden-angle radial MRI with reconstruction of extra motion-state dimensions using compressed sensing. *Magn. Reson. Med.* 2016; 75:775–788.
- [38] Uecker M, Hohage T, Block KT, Frahm J. Image reconstruction by regularized nonlinear inversion-joint estimation of coil sensitivities and image content. *Magn. Reson. Med.* 2008; 60:674–682.
- [39] Bakushinsky AB, Kokurin MY, “Iterative Methods for Approximate Solution of Inverse Problems”, *Mathematics and Its Applications*. Springer Science & Business Media, 2005.
- [40] Boyd S, Parikh N, Chu E, Peleato B, Eckstein J. Distributed Optimization and Statistical Learning via the Alternating Direction Method of Multipliers. *Found. Trends Mach. Learn.* 2011; 3:1–122.
- [41] Roeloffs V, Voit D, Frahm J. Spoiling without additional gradients: Radial FLASH MRI with randomized radiofrequency phases. *Magn. Reson. Med.* 2016; 75:2094–2099.
- [42] Barral JK, Gudmundson E, Stikov N, EtezadiAmoli M, Stoica P, Nishimura DG. A robust methodology for in vivo T1 mapping. *Magn. Reson. Med.* 2010; 64:1057–1067.
- [43] Uecker M, Ong F, Tamir JI, Bahri D, Virtue P, Cheng JY, Zhang T, Lustig M. Berkeley advanced reconstruction toolbox. In: *Proc. Intl. Soc. Mag. Reson. Med., Toronto, 2015*. p. 2486.
- [44] Rosenzweig S, Holme HCM, Uecker M. Simple auto-calibrated gradient delay estimation from few spokes using Radial Intersections (RING). *Magn. Reson. Med.* 2019; 81:1898–1906.
- [45] Uecker M, Zhang S, Frahm J. Nonlinear inverse reconstruction for real-time MRI of the human heart using undersampled radial FLASH. *Magn. Reson. Med.* 2010; 63:1456–1462.
- [46] Pearson TA, Blair SN, Daniels SR, Eckel RH, Fair JM, Fortmann SP, Franklin BA, Goldstein LB, Greenland P, Grundy SM et al. AHA guidelines for primary prevention of cardiovascular disease and stroke: 2002 update: consensus panel guide to comprehensive risk reduction for adult patients without coronary or other atherosclerotic vascular diseases. *Circulation* 2002; 106:388–391.
- [47] Sumpf T, Unterberger M. arrayshow: a guide to an open source matlab tool for complex MRI data analysis. In: *Proc. Intl. Soc. Mag. Reson. Med., Salt Lake City, 2013*. p. 2719.

- [48] von Knobelsdorff-Brenkenhoff F, Prothmann M, Dieringer MA, Wassmuth R, Greiser A, Schwenke C, Niendorf T, Schulz-Menger J. Myocardial T1 and T2 mapping at 3 T: reference values, influencing factors and implications. *J. Cardiovasc. Magn. Reson.* 2013; 15:1–11.
- [49] Kellman P, Herzka DA, Hansen MS. Adiabatic inversion pulses for myocardial T1 mapping. *Magn. Reson. Med.* 2014; 71:1428–1434.
- [50] Serry FM, Ma S, Mao X, Han F, Xie Y, Han H, Li D, Christodoulou AG. Dual flip-angle IR-FLASH with spin history mapping for B1+ corrected T1 mapping: Application to T1 cardiovascular magnetic resonance multi-tasking. *Magn. Reson. Med.* 2021; 86:3182–3191.
- [51] Cheng JY, Hanneman K, Zhang T, Alley MT, Lai P, Tamir JI, Uecker M, Pauly JM, Lustig M, Vasanawala SS. Comprehensive motion-compensated highly accelerated 4D flow MRI with ferumoxytol enhancement for pediatric congenital heart disease. *J. Magn. Reson. Imaging* 2016; 43:1355–1368.
- [52] Cheng JY, Zhang T, Alley MT, Uecker M, Lustig M, Pauly JM, Vasanawala SS. Comprehensive Multi-Dimensional MRI for the Simultaneous Assessment of Cardiopulmonary Anatomy and Physiology. *Sci. Rep.* 2017; 7:5330.
- [53] DiSopra L, Piccini D, Coppo S, Stuber M, Yerly J. An automated approach to fully self-gated free-running cardiac and respiratory motion-resolved 5D whole-heart MRI. *Magn. Reson. Med.* 2019; 82:2118–2132.
- [54] Hansen MS, Sørensen TS, Arai AE, Kellman P. Retrospective reconstruction of high temporal resolution cine images from real-time MRI using iterative motion correction. *Magn. Reson. Med.* 2012; 68:741–750.
- [55] Qi H, Fuin N, Cruz G, Pan J, Kuestner T, Bustin A, Botnar RM, Prieto C. Non-rigid respiratory motion estimation of whole-heart coronary MR images using unsupervised deep learning. *IEEE Trans. Med. Imaging* 2020; 40:444–454.
- [56] Hammernik K, Klatzer T, Kobler E, Recht MP, Sodickson DK, Pock T, Knoll F. Learning a variational network for reconstruction of accelerated MRI data. *Magn. Reson. Med.* 2018; 79:3055–3071.
- [57] Hermann I, Uhrig T, Chacon-Caldera J, Akçakaya M, Schad LR, Weingärtner S. Towards measuring the effect of flow in blood T1 assessed in a flow phantom and in vivo. *Phys. Med. Biol.* 2020; 65:095001.

## Supporting Information

Table 1: **Supporting Information Table S1.**  $T_1$  relaxation times (ms, mean  $\pm$  SD) and CoV values (%) for the experimental phantom in Figure 2.

		Tube 1		Tube 2		Tube 3		Tube 4		Tube 5		Tube 6	
		$T_1$	CoV	$T_1$	CoV	$T_1$	CoV	$T_1$	CoV	$T_1$	CoV	$T_1$	CoV
Delay 5 s	Look-Locker	290 $\pm$ 4	1.4 %	433 $\pm$ 5	1.2 %	601 $\pm$ 5	0.8 %	768 $\pm$ 7	0.9 %	1122 $\pm$ 15	1.3 %	1419 $\pm$ 21	1.5 %
	Proposed	312 $\pm$ 4	1.3 %	456 $\pm$ 5	1.1 %	623 $\pm$ 6	1.0 %	792 $\pm$ 6	0.8 %	1151 $\pm$ 13	1.1 %	1472 $\pm$ 21	1.4 %
Delay 4 s	Look-Locker	290 $\pm$ 4	1.4 %	432 $\pm$ 5	1.2 %	603 $\pm$ 6	1.0 %	768 $\pm$ 7	0.9 %	1111 $\pm$ 12	1.1 %	1386 $\pm$ 22	1.6 %
	Proposed	311 $\pm$ 4	1.3 %	455 $\pm$ 5	1.1 %	625 $\pm$ 6	1.0 %	793 $\pm$ 6	0.8 %	1151 $\pm$ 13	1.1 %	1466 $\pm$ 23	1.6 %
Delay 3 s	Look-Locker	290 $\pm$ 3	1.0 %	432 $\pm$ 5	1.2 %	600 $\pm$ 6	1.0 %	760 $\pm$ 8	1.1 %	1080 $\pm$ 11	1.0 %	1325 $\pm$ 18	1.4 %
	Proposed	311 $\pm$ 4	1.3 %	454 $\pm$ 5	1.1 %	622 $\pm$ 8	1.3 %	786 $\pm$ 8	1.0 %	1143 $\pm$ 12	1.0 %	1459 $\pm$ 25	1.7 %
Delay 2 s	Look-Locker	289 $\pm$ 3	1.0 %	430 $\pm$ 5	1.2 %	592 $\pm$ 6	1.0 %	740 $\pm$ 8	1.1 %	1015 $\pm$ 13	1.3 %	1215 $\pm$ 17	1.4 %
	Proposed	310 $\pm$ 4	1.3 %	453 $\pm$ 5	1.1 %	621 $\pm$ 7	1.1 %	788 $\pm$ 9	1.1 %	1142 $\pm$ 17	1.5 %	1457 $\pm$ 33	2.3 %
Delay 1 s	Look-Locker	286 $\pm$ 4	1.4 %	412 $\pm$ 5	1.2 %	549 $\pm$ 5	0.9 %	667 $\pm$ 7	1.0 %	779 $\pm$ 12	1.5 %	989 $\pm$ 15	1.5 %
	Proposed	308 $\pm$ 4	1.3 %	445 $\pm$ 5	1.1 %	608 $\pm$ 9	1.5 %	755 $\pm$ 9	1.2 %	1123 $\pm$ 25	2.2 %	1423 $\pm$ 65	4.6 %
IR Spin-Echo		312 $\pm$ 6	1.9 %	490 $\pm$ 8	1.6 %	653 $\pm$ 6	0.9 %	812 $\pm$ 8	1.0 %	1175 $\pm$ 10	0.9 %	1488 $\pm$ 16	1.1 %

Table 2: **Supporting Information Table S2.**  $T_1$  relaxation times (ms, mean  $\pm$  SD) and CoV values (%) for the experimental phantom in Figure 3.

	Tube 1		Tube 2		Tube 3		Tube 4		Tube 5		Tube 6	
	$T_1$	CoV	$T_1$	CoV	$T_1$	CoV	$T_1$	CoV	$T_1$	CoV	$T_1$	CoV
$\ell_1$ -Wavelet (0.005)	302 $\pm$ 8	2.6 %	444 $\pm$ 13	2.9 %	611 $\pm$ 15	2.5 %	783 $\pm$ 21	2.7 %	1148 $\pm$ 43	3.7 %	1457 $\pm$ 70	4.8 %
$\ell_1$ -Wavelet (0.02)	303 $\pm$ 7	2.3 %	444 $\pm$ 9	2.0 %	611 $\pm$ 10	1.6 %	783 $\pm$ 13	1.7 %	1144 $\pm$ 24	2.1 %	1454 $\pm$ 33	2.3 %
$\ell_1$ -Wavelet + Spatio-Temporal TV (0.005)	311 $\pm$ 5	1.6 %	451 $\pm$ 4	1.0 %	611 $\pm$ 4	0.7 %	786 $\pm$ 4	0.5 %	1144 $\pm$ 8	0.7 %	1454 $\pm$ 15	1.0 %
IR Spin-Echo	312 $\pm$ 6	1.9 %	490 $\pm$ 8	1.6 %	653 $\pm$ 6	0.9 %	812 $\pm$ 8	1.0 %	1175 $\pm$ 10	0.9 %	1488 $\pm$ 16	1.0 %

Table 3: **Supporting Information Table S3.** The P-value of paired t-test comparison of the proposed motion-resolved model-based reconstructed diastolic  $T_1$  values and the MOLLI values in each AHA segment for all scans.

	Anterior	Septal		Inferior	Lateral	
		Anteroseptal	Inferoseptal		Inferolateral	Anterolateral
Basal*	0.92	0.85	0.77	0.35	0.06	0.18
Middle	0.56	0.22	0.30	0.49	< 0.01	< 0.01
Apical	0.39	0.27		0.77	0.60	

\* Basal and apical results are from six subjects, while the mid-ventricular results are evaluated on all eleven subjects.

Table 4: **Supporting Information Table S4.** The relative difference (%) of the left-ventricular area between end-diastolic and end-systolic mid-ventricular myocardial  $T_1$  maps for all subjects and scans.

Subject	#1	#2	#3	#4	#5	#6	#7	#8	#9	#10	#11	mean $\pm$ SD
Scan #1	57	57	58	68	65	57	68	65	63	65	54	62 $\pm$ 5
Scan #2	60	54	59	65	62	54	67	57	68	65	55	61 $\pm$ 5

# Supporting Information File

## 1 Derivation of $T_1$ Estimation Formula From Incomplete (Partial) Recovery

To describe the effect of partial recovery, we split the recovery curve into two parts: The imaging part (subject to  $R_1^*$  relaxation) with a time period of  $t_{1s}$  and the free recovery part (subject to  $R_1$  relaxation) with a period of  $t_1$ . The dynamics of each part is then governed by:

$$\begin{aligned} \text{Imaging : } & M_{ss} - (M_{ss} - M_{ini}) \cdot e^{-R_1^* \cdot t_{1s}} =: A_1 + B_1 M_{ini} \\ \text{Free relaxation : } & M_0 - (M_0 - M_{ini}) \cdot e^{-R_1 \cdot t_1} =: A_2 + B_2 M_{ini} \end{aligned}$$

where  $t_{1s}$  and  $t_1$  are the time periods for imaging and free relaxation parts, respectively.

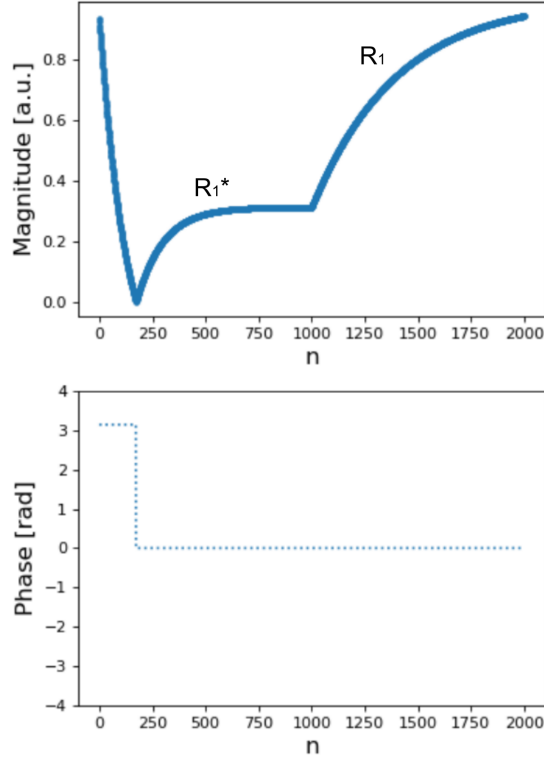


Figure 1: Demonstration of IR Look-Locker signal with partial recovery: 3 s imaging followed by 3 s free recovery. n describes the index of the RF excitation.

The joint effects of these two blocks can then be written as:  
 free relaxation after imaging:  $A_2 + B_2(A_1 + B_1 M_{ini}) =: A_3 + B_3 M_{ini}$   
 where  $A_3 = A_2 + B_2 A_1$  and  $B_3 = B_2 B_1$

For the new signal model, we simply have to find the fix point which gets mapped to itself by both

relaxation parts and the inversion:

$$\begin{aligned}
M'_0 &= A_3 + B_3 \cdot (-M'_0) \\
\Rightarrow M'_0 &= \frac{A_3}{1 + B_3} \\
&= \frac{A_2 + B_2 A_1}{1 + B_2 B_1} \\
&= \frac{M_0(1 - e^{-R_1 \cdot t_1}) + e^{-R_1 \cdot t_1} M_{ss}(1 - e^{-R_1^* \cdot t_{1s}})}{1 + e^{-R_1 \cdot t_1} \cdot e^{-R_1^* \cdot t_{1s}}}
\end{aligned}$$

By substituting  $M_0 = R_1^{-1} M_{ss} R_1^*$ , we obtain the formula of equation (1) in the main manuscript.

Therefore, the key idea is that even with partial recovery, the signal is still mono-exponential and can be fitted with a 3-parameter model

$$s(t) = M_{ss} - (M_{ss} + M'_0) \cdot e^{-t \cdot R_1^*}$$

Following parameter estimation, accurate  $T_1$  can be achieved using equation (1) in the main manuscript in a post-processing step.

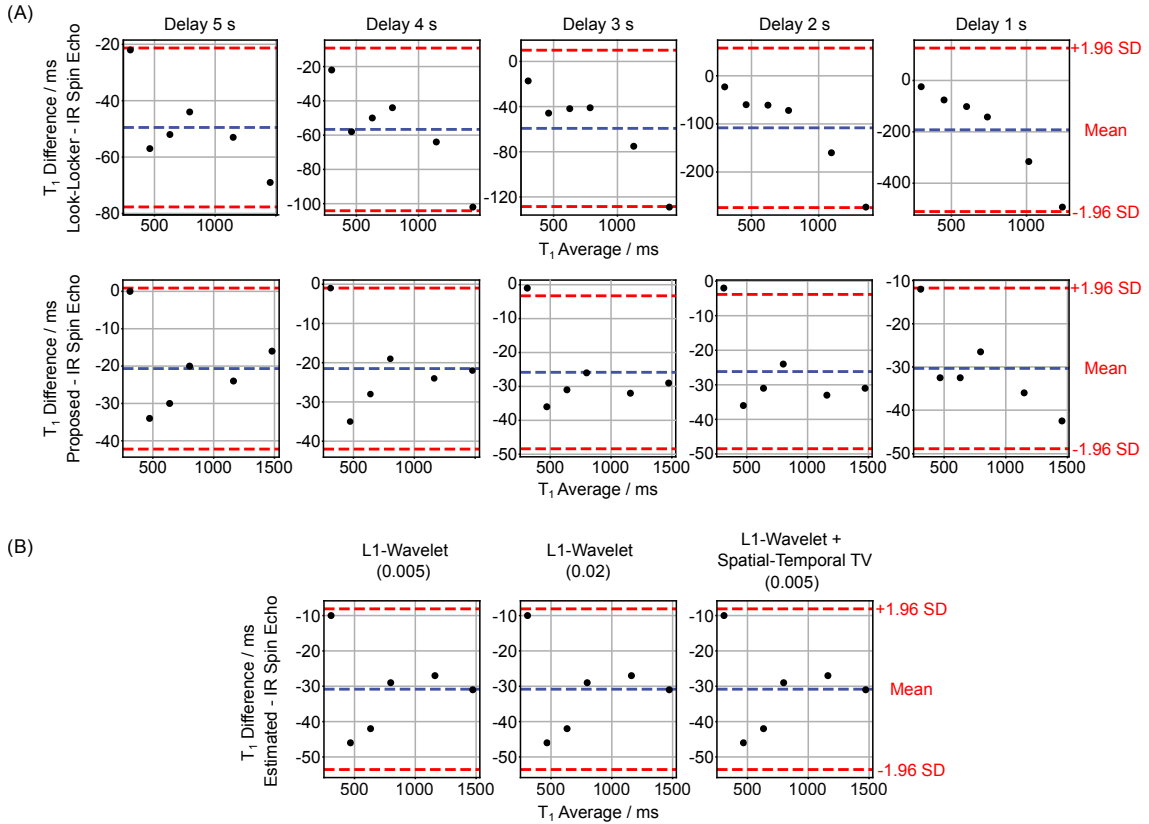


Figure 2: **Supporting Information Figure S1.** A. Bland-Altman plots comparing ROI-analyzed phantom  $T_1$  values (top) between the original Look-Locker correction and the IR spin-echo reference (from left to right, mean difference: -50, -57, -74, -108 and -195 ms, and SD: 14, 24, 45, 85 and 163 ms), and (bottom) between the proposed correction and the IR spin-echo reference (from left to right, mean difference: -21, -22, -26, -26 and -41 ms, and SD: 11, 10, 12, 11 and 19 ms) for various delays. B. Bland-Altman plots comparing ROI-analyzed phantom  $T_1$  values between motion-resolved model-based reconstruction with different regularizations and the IR spin-echo reference (from left to right, mean difference: -31, -31 and -31 ms, and SD: 12, 12 and 12 ms).

## 2 Study of High-Dimensional Regularization on Simulated Dynamic Phantoms

To study the effects of various regularization types (explained in the Iterative Reconstruction part of the Methods section) in the motion-resolved reconstruction in general, a numerical motion phantom consisting of three elliptical objects was simulated. The diameters of the centered two objects were designed to change along time, mimicking the cardiac contraction motion, moving from diastolic to systolic phase. Moreover, three small tubes, representing certain "lesions", are added to the "myocardium" region. The corresponding k-space data was then derived from the analytical Fourier representation of ellipses assuming an array of eight circular receiver coils surrounding the phantom without overlap. The simulation employed a continuous radial FLASH acquisition with a tiny golden-angle ( $\approx 23, 63^\circ$ ) between successive spokes, base resolution of 256 pixels covering a field of view of 192 mm, 15 spokes per frame and a total of 32 time frames.

The effects of different regularizations were tested on the simulated dynamic phantom using motion-resolved image reconstruction ("PICS" command) in BART. The Supporting Information Figure S2 presents such a comparison where all reconstructions have employed the same regularization parameter. Certain streaking artifacts appear in the images when only the  $\ell_1$ -Wavelet-based spatial regularization is applied. Moreover, the reconstructed images are blurred with signal inhomogeneities on the myocardium regions. The above artifacts can be largely removed with the use of temporal TV regularization. However, the pure TV regularization also introduced the "line"-like artifacts along the time dimension, as shown in the line profile images. The joint  $\ell_1$ -Wavelet and temporal TV regularization helps to reduce such artifacts but still has some "line"-like artifacts presented in the line profiles. The spatio-temporal TV regularization, which takes account of both spatial and temporal information into the TV regularization, plus the  $\ell_1$ -Wavelet spatial regularization largely eliminate all the above artifacts, resulting in both smooth images and line profiles.

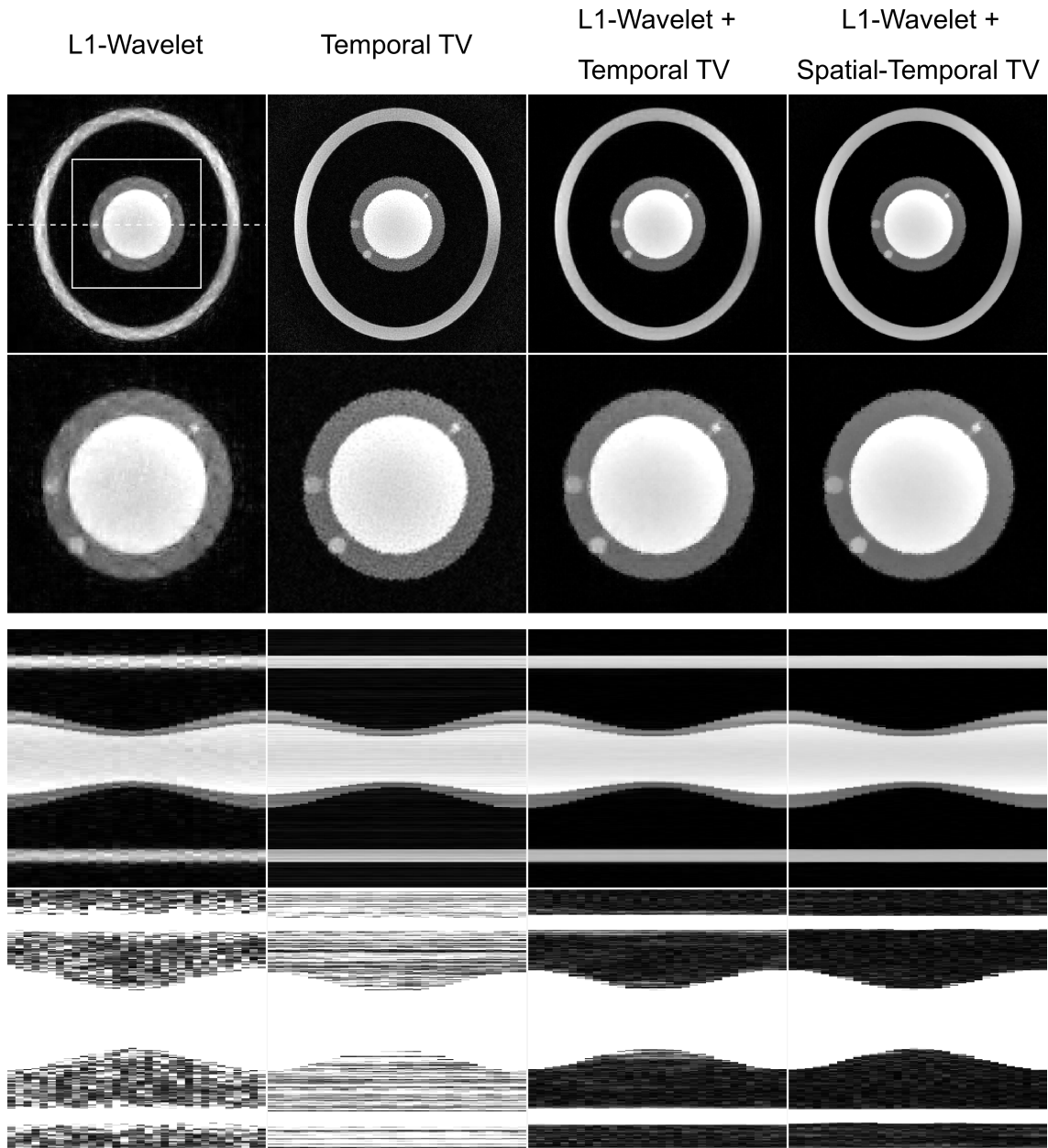


Figure 3: **Supporting Information Figure S2.** (Top) One of the "end-diastolic" images (28th of 32) of a simulated dynamic image series and (middle and bottom) the corresponding horizontal profiles (dashed line in the top) through the motion dimension. The image series were reconstructed using the motion-resolved image reconstruction with different regularization type.

### 3 Supporting Information for In Vivo Studies

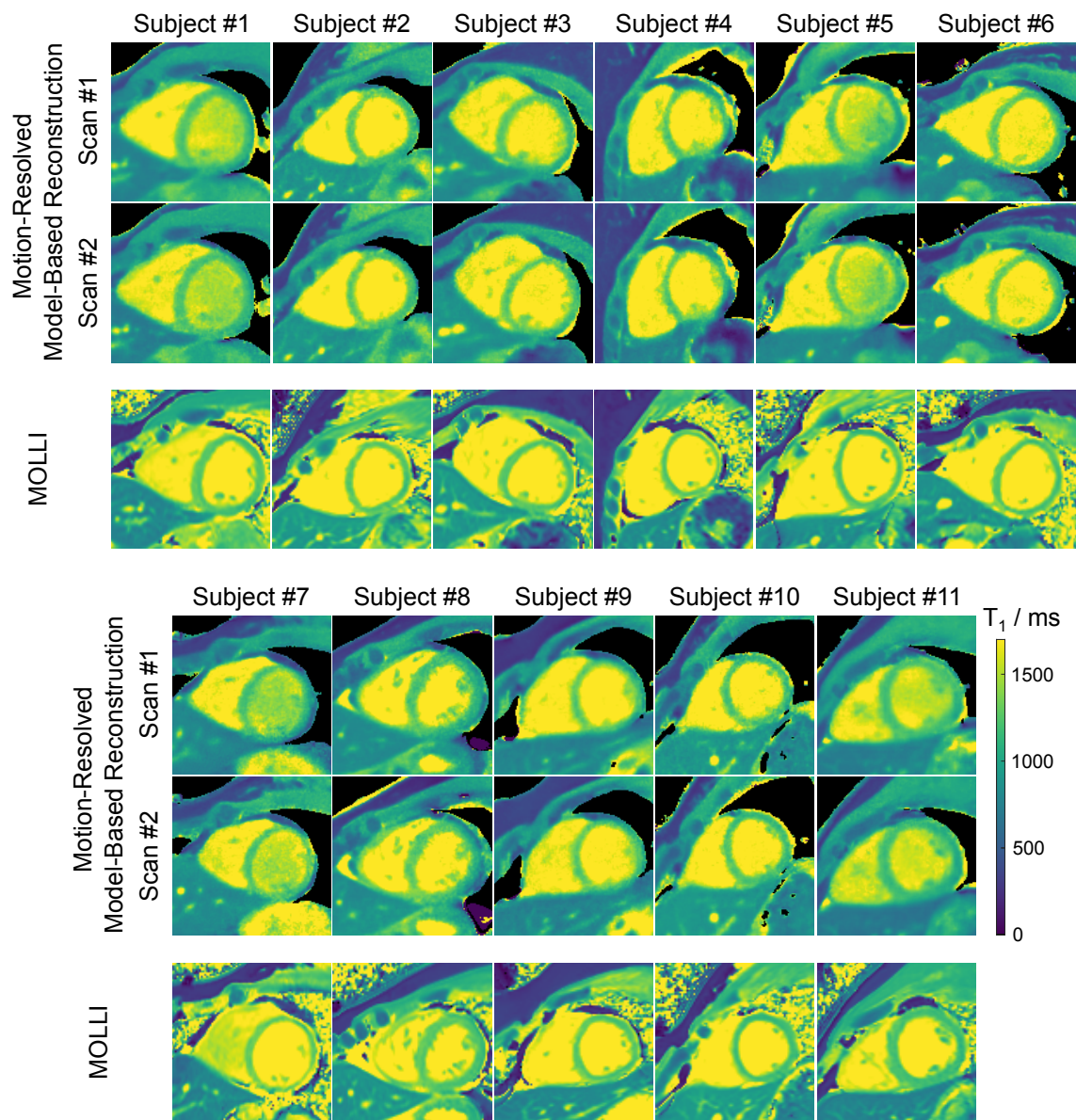


Figure 4: **Supporting Information Figure S3.** Two repeated myocardial  $T_1$  maps (end-expiration, end-diastolic) of the motion-resolved model-based reconstruction acquired during free breathing in comparison to MOLLI acquired in a breathhold for all eleven subjects.

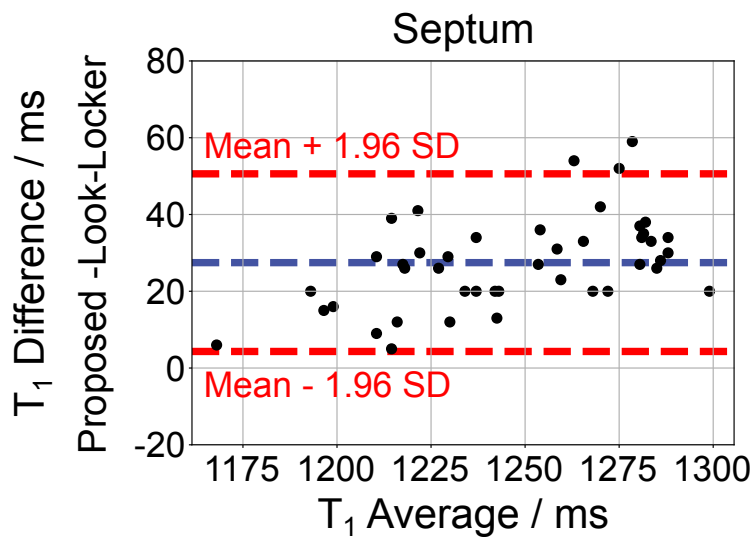


Figure 5: **Supporting Information Figure S4.** Bland-Altman plots comparing ROI-analyzed mid-ventricular septal mean  $T_1$  values between the proposed correction and the Look-Locker correction for all subjects and scans. The mean difference is 28 ms and SD is 12 ms.

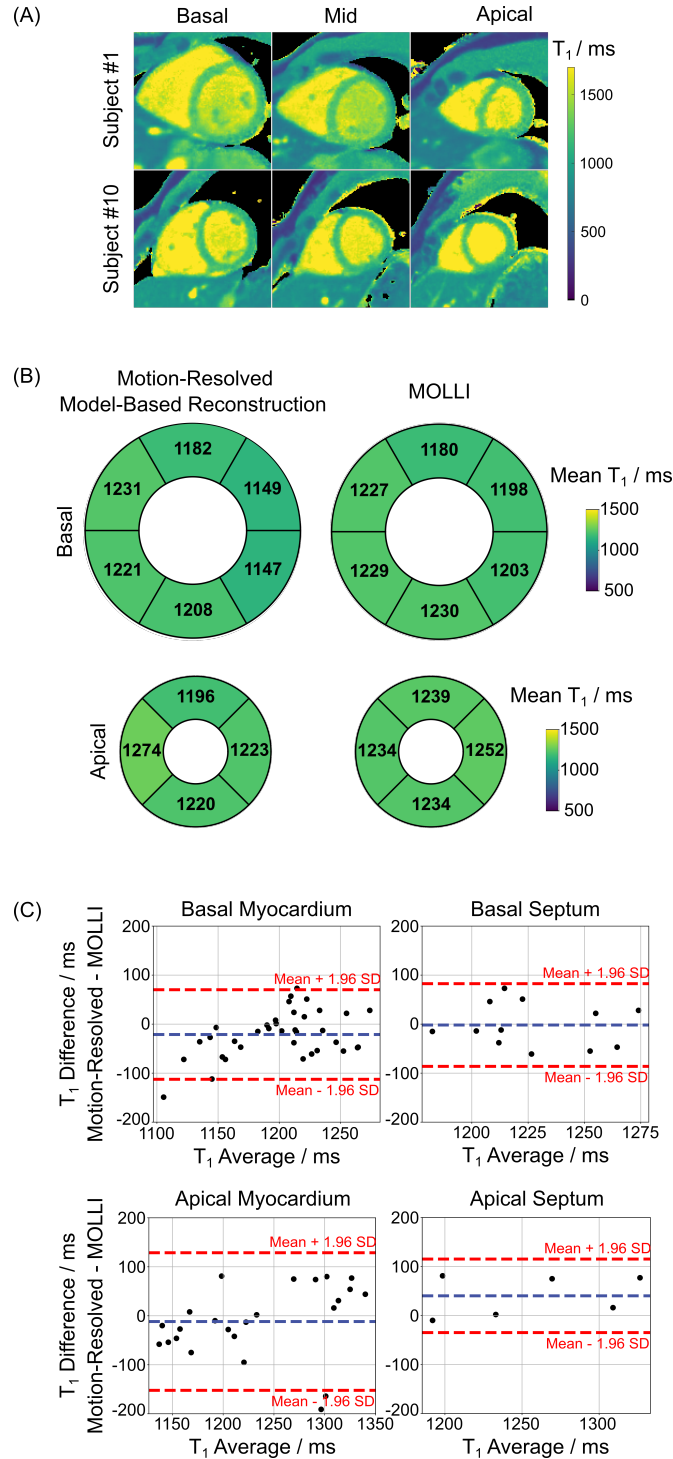


Figure 6: **Supporting Information Figure S5.** A. Representative diastolic  $T_1$  maps of basal, mid and apical short-axis slices reconstructed with the motion-resolved model-based reconstruction (free breathing) for two healthy subjects. B. Bullseye plots of (top) six basal segments and (bottom) four apical segments, showing the mean diastolic  $T_1$  values for six subjects for (left) the motion-resolved model-based reconstruction acquired during free breathing and (right) the MOLLI reference acquired in a breathhold. C. Bland-Altman plots comparing (top) the mean diastolic  $T_1$  values of all six basal segments (mean difference: -21 ms, SD: 47 ms) and the two basal septal segments (segments 2 and 3 according to AHA, mean difference: -2 ms, SD: 43 ms), and (bottom) the mean diastolic  $T_1$  values of all apical segments (mean difference: -12 ms, SD: 72 ms) and the one apical septal segment (segment 14 according to AHA, mean difference: 40 ms, SD: 38 ms) for the proposed method and MOLLI for six subjects.

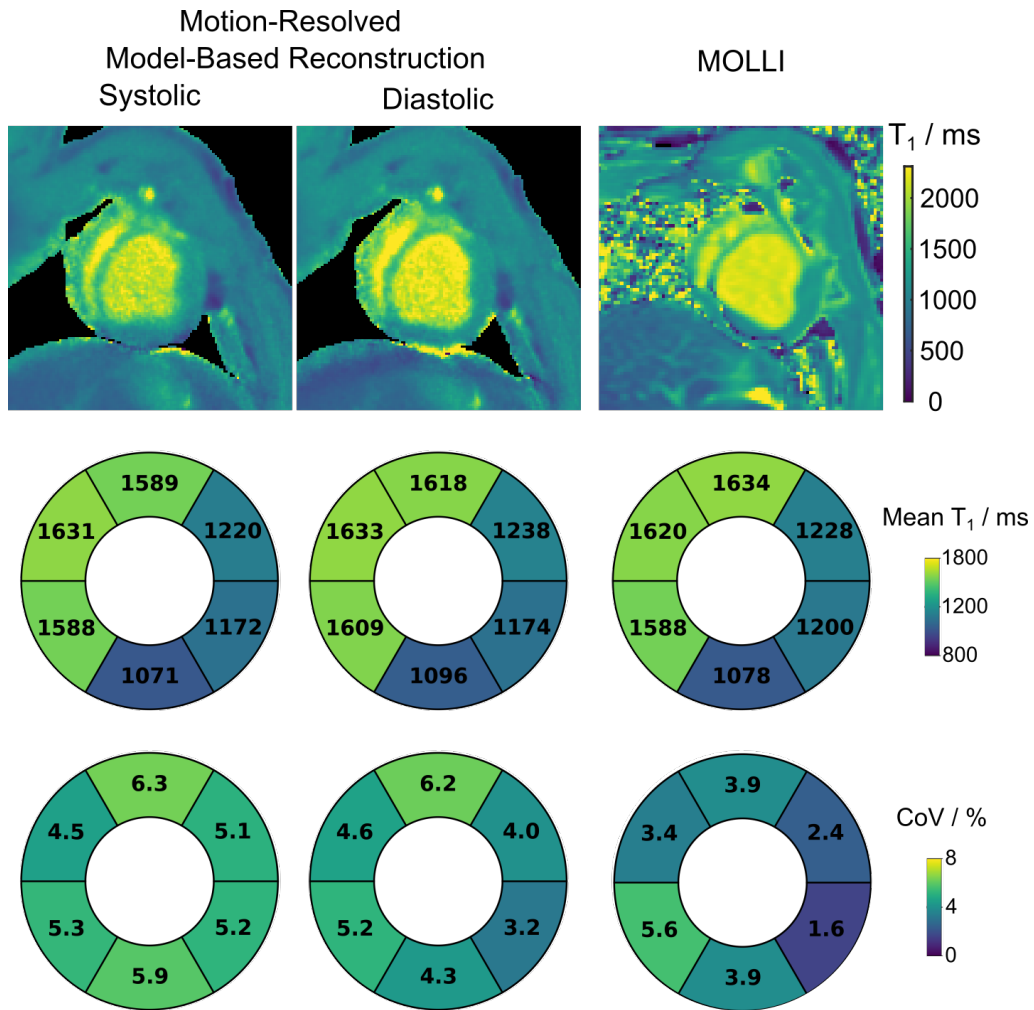


Figure 7: **Supporting Information Figure S6.** Free-breathing systolic and diastolic myocardial  $T_1$  maps reconstructed with the motion-resolved model-based reconstruction and their comparison to the MOLLI reference for a pig study. The ROI-analyzed mean  $T_1$  values (ms) and CoV values (%) for all the mid-ventricular AHA segments are presented in the bottom.

**Supporting Information Video S1.** Synthesized  $T_1$ -weighted image series (bright blood and dark blood) and the corresponding myocardial  $T_1$  maps through the cardiac phase dimension for subject #2.

**Supporting Information Video S2.** Synthesized  $T_1$ -weighted image series (bright blood and dark blood) and the corresponding myocardial  $T_1$  maps through the cardiac phase dimension for subject #3.

**Supporting Information Video S3.** Synthesized  $T_1$ -weighted image series at temporal resolution of 49 ms for all inversion times and all cardiac phases of subject #2.